

FACULTY FOR PHYSICS AND ASTRONOMY

UNIVERSITY OF HEIDELBERG

Diploma Thesis

in Physics
submitted by

Dirk Krumbhorn

born in Bad Friedrichshall

2008

**Study of J/ψ production in $p + p$
collisions at $\sqrt{s} = 10$ TeV with the
Transition Radiation Detector of ALICE**

**This diploma thesis has been carried out by Dirk Krumbhorn at the
Physikalisches Institut
under the supervision of
Helmholtz Young Investigator
Dr. Kai Schweda**

Study of J/ψ production in $p + p$ collisions at $\sqrt{s} = 10$ TeV with the Transition Radiation Detector of ALICE

Within this thesis, the performance of J/ψ -production in $p+p$ collisions at $\sqrt{s} = 10$ TeV with the central barrel detectors in ALICE was studied. In particular, the decay channel $J/\psi \rightarrow e^+ + e^-$ ($BR \approx 6\%$) with the electron and positron identified by the Transition Radiation Detector (TRD) using full-blown Monte Carlo simulations was examined. Influences of different cuts on reconstructed single tracks as well as the particle identification framework for the TRD in AliRoot were carefully studied. The obtained overall J/ψ reconstruction efficiency at mid-rapidity $|y| < 0.9$ is $\epsilon \approx 0.12$. The J/ψ is reconstructed with a mass resolution of $\sigma \approx 40$ MeV/ c^2 at a signal to background ratio of 0.6. These results are in good agreement with earlier studies using fast simulations and parameterised functions for the detector response. In 10^9 $p+p$ collisions, corresponding to one year of data taking with ALICE and full TRD, J/ψ production can be addressed.

Untersuchung der J/ψ Produktion in $p + p$ Kollisionen bei $\sqrt{s} = 10$ TeV mit dem Übergangsstrahlungsdetektor von ALICE

Im Rahmen dieser Arbeit wurde die J/ψ -Produktion in $p+p$ Kollisionen bei $\sqrt{s} = 10$ TeV mit den zentralen Detektoren von ALICE untersucht. Insbesondere wurde der Zerfallskanal $J/\psi \rightarrow e^+ + e^-$ ($BR \approx 6\%$), bei dem Elektronen und Positronen mit dem Übergangs-Strahlung-Detektor (TRD) identifiziert wurden, unter der Verwendung voller Monte Carlo Simulationen untersucht. Die Einflüsse verschiedener Bedingungen an die rekonstruierten Spuren einzelner Teilchen, sowie das Teilchenidentifikationssystem des TRD in AliRoot sind genau untersucht worden.

Die erhaltene durchschnittliche J/ψ Rekonstruktionseffizienz bei mittleren Rapiditäten von $|y| < 0.9$ ist $\epsilon \approx 0.12$. Das J/ψ -Meson wird mit einer Massenauflösung von $\sigma \approx 40$ MeV/ c^2 bei einem Signal zu Untergrund Verhältnis von 0.6 rekonstruiert. Diese Ergebnisse sind in guter Übereinstimmung mit früheren Studien mit "fast simulations" und parameterisierten Funktionen der Detektorantwort.

In 10^9 $p+p$ Kollisionen, entsprechend einem Jahr Datenaufnahme mit ALICE und vollständigem TRD, kann die J/ψ Produktion bestimmt werden.

Contents

1. Introduction	1
2. Quantum Chromo Dynamics and the J/ψ meson	5
2.1. Lattice Quantum Chromo Dynamics	5
2.2. Heavy Quark Potential	9
2.3. The J/ψ meson	11
3. LHC and ALICE	15
3.1. The Large Hadron Collider	15
3.2. A Large Ion Collider Experiment	19
4. The Transition Radiation Detector	23
4.1. Energy Loss of Charged Particles	23
4.2. Detector Design	26
4.3. Charged Particle Identification	29
5. ALICE Offline Framework	37
5.1. Overview	37
5.2. Monte Carlo Simulations	37
5.3. Track Reconstruction in the Central Barrel	39
6. J/ψ Analysis	45
6.1. J/ψ Monte Carlo Input	45
6.2. Single Track Selection	51
6.3. Invariant Mass Calculation	57
6.4. Efficiency Studies	61
6.5. Resolution	66
6.6. Background	69
7. Summary and Outlook	75
Bibliography	76

1. Introduction

Quantum chromo dynamics (QCD) is the theory of strong interactions between colour carrying particles (quarks, gluons). Asymptotic freedom [1, 2] is a remarkable feature of QCD, i.e. the interaction between quarks weakens as quarks get closer to one another. Shortly after the idea of asymptotic freedom was introduced, it was realized that this has a fascinating consequence. Above a critical temperature and density, quarks and gluons are freed from their hadronic boundary forming a deconfined phase of matter [3, 4] -a quark gluon plasma (QGP). Our present world exists at low temperatures and densities with quarks and gluons confined to the size of hadrons. But shortly after its origin, our universe was of much higher temperature and density. About $10 \mu s$ after the Big Bang, it is thought that all matter visible today existed as a quark gluon plasma. Solving QCD in regularised lattice calculations, at vanishing or finite net-baryon density, predicts a cross-over transition from the deconfined thermalised partonic matter to hadronic matter at a critical temperature $T_c \approx 150 - 190 MeV$ [5].

A similar value has been derived in the 1960s by R. Hagedorn as the limiting temperature for hadrons when investigating hadronic matter [6]. The only way to create and study such a QGP in the laboratory, is the collision of heavy nuclei at highest center-of-mass energies. A crucial question is to what extent matter is created in these collisions, i.e. whether local equilibrium is achieved. If the system reaches equilibrium at least approximately, then temperature, pressure, energy and entropy density can be defined. The relation amongst these macroscopic parameters is given by the (partonic) equation of state. Heavy-flavor (c, b) quarks are excellent tools to study the degree of thermalisation of the initially created matter [7]. As shown in Fig.1.1, the large masses of heavy quarks are almost exclusively generated through their coupling to the Higgs field in the electro-weak sector, while masses of light quarks (u, d, s) are dominated by spontaneous breaking of chiral symmetry in QCD. This means that in a QGP, where chiral symmetry might be restored, light quarks are left with their bare current masses while heavy-flavor quarks remain heavy. Due to their large masses, $m = m_{c,b} \gg \Lambda_{QCD}$, heavy quarks are dominantly created in early stage perturbative QCD processes. The overall number of heavy quarks is conserved since their heavy mass is much larger than the maximum temperature of the medium. Thus thermal production is negligible. Also, cross sections for heavy quark-antiquark annihilation are marginal [8]. Frequent interactions at the partonic stage will cause these heavy quarks to participate in collective motion [9, 10, 11] and finally kinetically equilibrate. This leads to the idea of statistical hadronization

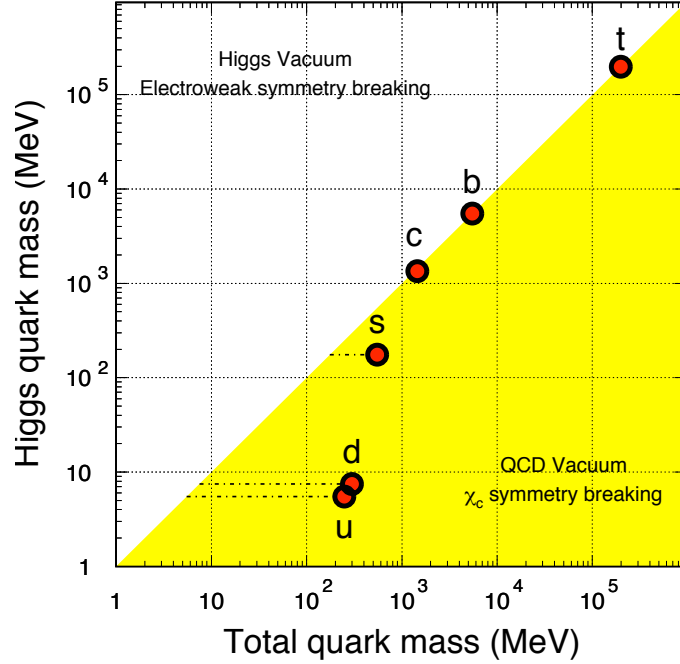


Figure 1.1.: Quark masses in the QCD vacuum and the Higgs vacuum. A large fraction of the light quark masses is due to chiral symmetry breaking in the QCD vacuum while heavy quarks attain almost all their mass from coupling to the Higgs field. This figure has been taken from [7].

of charm quarks [12]. Calculations predict significant changes in the production of hidden charm hadrons, e.g. J/ψ [13]. Quarkonia play a key role in research into the quark gluon plasma. In 1986, Satz and Matsui [14] suggested that the high density of gluons in a quark gluons plasma should destroy charmonium systems, in a process analogous to Debye screening of the electromagnetic field in a plasma through the presence of electric charges. Such a suppression was indeed observed by the NA50 collaboration [15] at the super proton synchrotron (SPS). However, absorption of charmonium in the cold nuclear medium also contributes to the observed suppression [16] and the interpretation of the SPS data remains inconclusive.

At high collider energies, the large number of charm-quark pairs produced leads to a new production mechanism for charmonium, either through statistical hadronization at the phase boundary [12, 17] or coalescence of charm quarks in the plasma [18, 19, 20, 21, 22]. At low energy, the average number of charm-quark pairs produced in a collision is much lower than one, implying that charmonium is always formed from this particular pair. If charm quarks are abundantly produced (in the order of some tens to a few hundred), charm quarks from different pairs can combine to form charmonium, see Fig.1.2. This mechanism works only if heavy charm quarks can propagate over substantial distance to meet their counterpart. Under these conditions, charmonium production scales quadratically with the number of charm quark pairs initially produced in the system [23]. Thus enhancement rather than strong suppression is predicted for high collision energies. This would be a clear

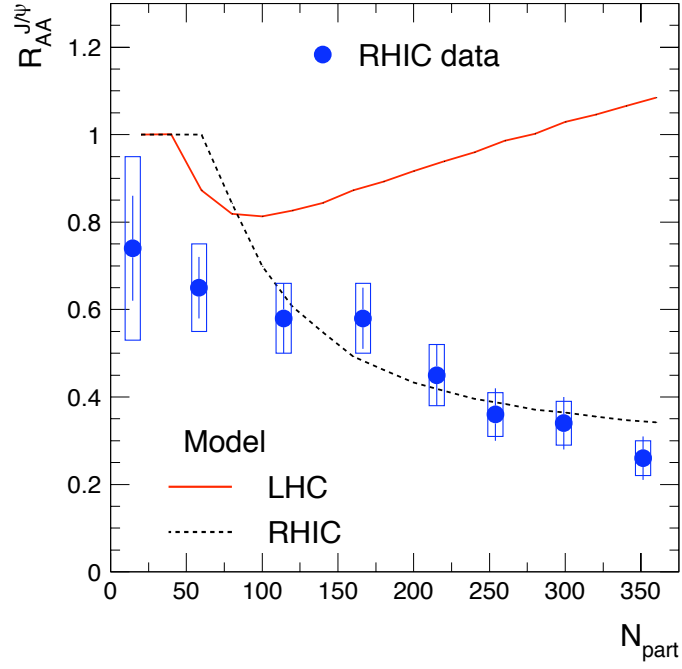


Figure 1.2.: Statistical Model predictions for charmonium production relative to normalised $p+p$ collisions for RHIC (dashed line) and LHC (solid line) energies. The data points are for top RHIC energies as measured by the PHENIX collaboration [24]. This figure has been taken from [23].

signature of the formation of a quark gluon plasma with deconfined charm quarks and thermalized light quarks. The dissociation of quarkonia is therefore taken as an indicator of the temperature reached in a QGP as illustrated in Fig. 1.3.

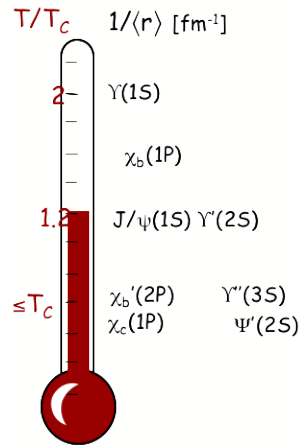


Figure 1.3.: Most recent results on quarkonia dissociation temperature in QGP as a thermometer. This figure has been taken from [25].

Due to the OZI rule, a significant fraction of 6% of the J/ψ mesons decay in the electro-magnetic channel to electron-positron pairs. Further, electrons do not interact strongly and are therefore not influenced by the formation of a QGP.

At high momentum, charm and bottom quarks propagating through the medium provide another tool for probing the medium, e.g. the gluon density [26]. Due to their large mass, novel effects have been predicted [27].

The Large Hadron Collider (LHC) at CERN near Geneva, Switzerland, will provide collisions of nuclei with masses up to that of lead. Unprecedented high center-of-mass energies up to $\sqrt{s_{NN}} = 5.5 \text{ TeV}$ per nucleon-nucleon pair for lead-lead collisions will be achieved. At these energies, heavy quarks are abundantly produced. Compared to the presently highest energies in nucleus-nucleus collisions achieved at the relativistic heavy ion collider (RHIC) at Brookhaven National Laboratory in Upton, New York, production of charm quarks (bottom quarks) is roughly ten times (100 times) larger at LHC.

The dominant fraction of charm quarks emerges in open charm hadrons, e.g. D-mesons, while hidden charm hadrons, e.g. J/ψ , carry roughly one percent of the total charm yield. Theoretical calculations have large uncertainties due to the poorly known gluon distribution in the low Feynman-x region relevant for LHC energies [28]. Thus, measurements on charm (bottom) production in $p+p$ or Pb+Pb collisions are essential. At RHIC, the STAR and PHENIX experiments have measured the charm production cross section for various collision energies and nucleus species [29].

At LHC, the ALICE experiment will measure most of the heavy quark hadrons. Open charm hadrons are identified with help of the inner tracking system (ITS) of ALICE. The ALICE transition radiation detector (TRD) measures production of J/ψ and other quarkonia by identifying electrons and positrons from electromagnetic decays over a large momentum range. Furthermore, the TRD provides fast trigger capabilities within $6 \mu\text{s}$ for particles at momentum above $3 \text{ GeV}/c$.

Within this thesis, the expected performance on J/ψ -production in $p+p$ collisions at $\sqrt{s} = 10 \text{ TeV}$ with ALICE was studied in the $J/\psi \rightarrow e^+ + e^-$ decay channel (BR=6%) using full-blown Monte Carlo simulations. The efficiency for extracting the J/ψ -signal as function of transverse momentum and pseudo-rapidity is studied in detail. An estimate on the combinatoric background from mis-identified hadrons, e.g. π, K, p is given.

This thesis is organised as follows. In Chap. 2 information on lattice QCD, its insight on the heavy quark potential and the J/ψ meson is provided. Chapter 3 gives a brief overview of the Large Hadron Collider and its four main experiments with a closer look at the ALICE detector. In Chap. 4 the particle identification in ALICE, in particular the electron identification with the Transition Radiation Detector as well as the detector design of the TRD is described. The ALICE offline framework and the data processing flow in simulation and the reconstruction are summarised in Chap.5. Chapter 6 presents the status of the study of the J/ψ meson reconstruction in the $e^+ + e^-$ decay channel and gives an estimate of the combinatoric background. A summary and outlook is given in Chap. 7.

2. Quantum Chromo Dynamics and the J/ψ meson

2.1. Lattice Quantum Chromo Dynamics

Since the coupling in strong interactions gets smaller with increasing energy, perturbation theory produces better results at high energies. Although this approach provides various insights into the qualitative features of the quark-gluon plasma, there are major drawbacks. On the one hand, perturbative results are by definition not exact. Additionally, higher order, $O(g^6)$ and beyond, contributions result in an infrared divergency [30]. Finally perturbative calculation does never reveal physics of a phase transition as it is intrinsically non-perturbative.

These difficulties are overcome with a method first proposed by Wilson in 1974. He proposed to discretise the continuous space-time of QCD by defining QCD on a discretised space-time lattice. The lattice formulation is achieved by introducing a four dimensional space-time hyper-cubic of size $N_\sigma^3 \times N_\tau$, where N_σ is the number of lattice point per spatial dimension and N_τ the amount of points in the temporal dimension. The distance between two neighbouring lattice points, the lattice spacing, is further referred to as the variable a . Visually spoken every lattice point is occupied by a quark or anti-quark (field) which “lives” only in one of these points. Gluons, i.e. the gauge fields, on the other hand are the links between two lattice points. The construction of the space time lattice is illustrated in Fig. 2.1

By correctly introducing the lattice formulation, a gauge invariant regularisation of the ultraviolet divergences is achieved and *non*-perturbative numerical simulations are possible. Hence, only the time span until an *exact* solution for a chosen *configuration* of input parameters is achieved, depends only on the computing power that is put into the calculations.

A comprehensive derivation of the theory of lattice Quantum Chromo Dynamics (lQCD) can be found e.g. in [30]. In the following only the lQCD results most important for this work are presented.

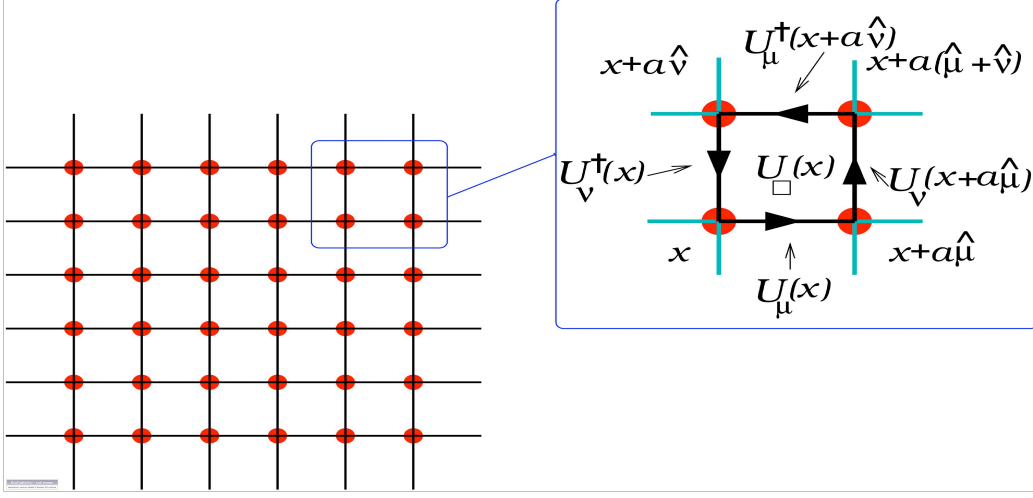


Figure 2.1.: Schematic design of IQCD. The quark and anti-quark fields live in the lattice points. This figure has been taken from [31].

Equation of State

If the thermodynamic system that describes the QGP reaches equilibrium at least approximately, the partition function, temperature, pressure p and energy density ϵ are defined. The relation amongst these macroscopic parameters are obtained in lattice QCD as:

$$\frac{p}{T^4} = \frac{1}{VT^3} \ln Z(T, V, \mu, \dots) \quad (2.1)$$

$$\frac{\epsilon - 3p}{T^4} = T \frac{d}{dT} \left(\frac{p}{T^4} \right)_{\text{fixed } \mu/T} \quad (2.2)$$

Where $Z(T, V, \mu, m_q, a, \dots)$ is the grand canonical partition function in its lattice formulation being the integral over the fundamental quark ($\bar{\psi}, \psi$) and gluon ($U \equiv U_{\mu\nu}(x)$) fields and the Euclidean action $S_E \equiv S_g + S_F$, containing a purely bosonic (S_g) and fermionic (S_F) contribution.

$$Z = \int [dU] [d\bar{\psi}d\psi] e^{-S_g(U) - S_F(\bar{\psi}, \psi, U)} \quad (2.3)$$

$$= \int [dU] \text{Det}F[U] e^{S_g(U)} \quad (2.4)$$

To get physical results, the lattice calculations are extrapolated to the thermodynamic limit, $V \rightarrow \infty$, $N \rightarrow \infty$, $N/V = \text{const}$ and continuum limit, $a \rightarrow 0$.

Equation (2.1) and Eq. (2.2) hence allow a detailed comparison of different computational schemes, e.g. numerical lattice calculations and analytic approaches in lattice calculations.

In the following only the case of vanishing chemical potential, $\mu = 0$, is considered since the focus is on the LHC and RHIC experiments at which the chemical potential is in good approximation zero. Additionally introduces a finite chemical potential difficulties in the lattice calculations.

Figure 2.2 shows the results for the pressure obtained from lattice calculations in units of T^4 against the temperature T in MeV . The purple line represents the pure gauge theory, $SU(3)$, $m_f = \infty$, extrapolated to the continuum limit. Consequently, no degrees of freedom in terms of light quarks are taken into account. The lattice results with a configuration of two (three) light quarks degenerated in mass are indicated in red (blue). The physical case of two mass degenerated light, up and down, quarks and one heavy quark, the strange quark, in green. The pressure rises at the vicinity of a critical temperature T_c due to the large increase in degrees of freedom (d.o.f.) from hadronic to partonic matter. In partonic matter the degrees of freedom are composed of spin, colour of quarks and gluons as well as quark flavour n_f , $g_{total} = g_q + g_g$; $g_q = 2_{spin} \cdot 3_{colour} \cdot n_f$, $g_g = 2_{spin} \cdot 8_{colour}$ compared to the d.o.f. in hadronic matter.

The critical temperature as well as the approached pressure values for a given temperature depend rather strong on the number of quark flavours, the number of degrees of freedom, respectively.

The arrows corresponding to each case indicate the Stefan-Boltzmann (SB) limit

$$\frac{\epsilon_{SB}}{T^4} = \frac{3p_{SB}}{T^4} = \left(16 + \frac{21}{2}n_f\right) \frac{\pi^2}{30} \quad (2.5)$$

of an ideal gas. Only about 80% of the SB limit are reached even for $T > 4 T_c$. Nevertheless if normalised to the Stefan-Boltzmann limit, right hand side of Fig. 2.2, the independence on the number of flavours is quite striking. The fact that the Stefan-Boltzmann limit is not reached shows that a QGP at temperatures even up to $4 \cdot T/T_c$ is not an ideal gas since quarks are not massless and point-like and further constant gluon interaction between quarks and gluons takes place.

However, most recent lattice results lead to critical temperatures of $T_c \approx 150 - 190$ MeV depending on the details of the calculations performed by the two major groups in this field around Fodor/Katz of the Budapest collaboration and Karsch of the Bielefeld collaboration.

The energy density rises more rapidly at the transition temperature than the pressure (Fig. 2.3). The same scenario is shown for two and three light quarks as well as for two light and one heavy quark. The transition takes place at $\epsilon/T_c^4 \simeq 6 \pm 2$. Although the corresponding value in the $SU(3)$ gauge theory, $\epsilon/T_c^4 \simeq 0.5$, differs by an order of magnitude, it is rather remarkable that the transition densities expressed in physical units are quite similar. With $T_c \approx 175$ MeV the resulting critical energy density is in this case $\epsilon_c \approx 0.7$ MeV/fm³.

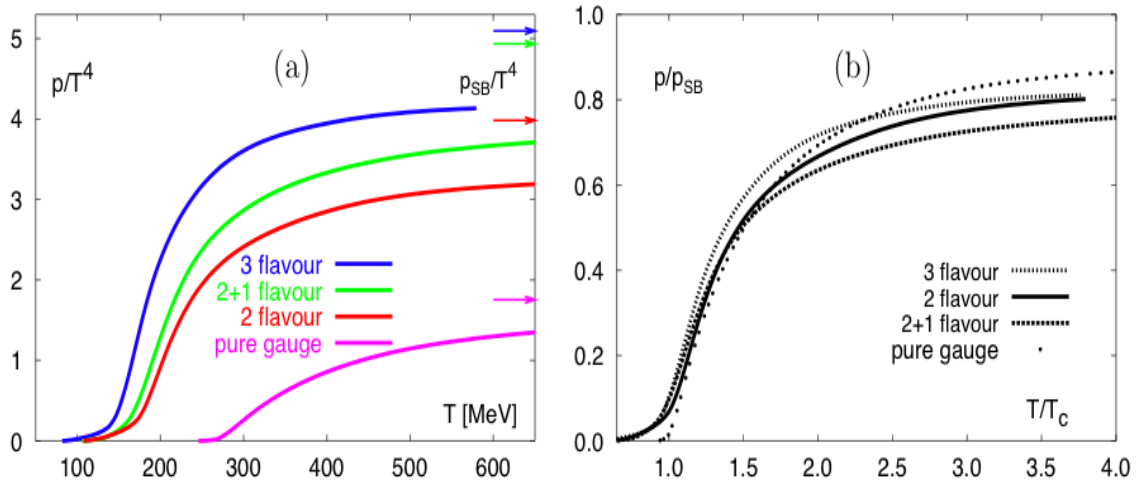


Figure 2.2.: The pressure in QCD with $n_f = 0, 2$ and 3 light quarks as well as two light and a heavier (strange) quark. In the case of the $SU(3)$ pure gauge theory the continuum extrapolated result is shown. The Arrows indicate the ideal gas pressure p_{SB} . This figure has been taken from [32].

The influence of the numbers of degrees of freedom is less explicit for the energy density than observed for the pressure since the change is compensated by the decrease of T_c .

The configuration presets for the shown lattice results for p and ϵ are: $N_\sigma = 16$ and $N_\tau = 4$ which already approximates the thermodynamic limit well. The light quark masses are $m_l/T = 0.4$ and the heavy quark mass $m_h/T = 1$. The non-physical quark masses are taken because the cost of computing power depends approximately exponential on the quark mass in the used configuration. To generate 1000 independent configurations for a rather large lattice of $N_\sigma^3 \times N_\tau = 24^3 \times 40$, $a = 0.08 fm$, with physical quark masses and a cluster of 10^{12} Floating point Operations Per Second, one year is needed [33].

The critical temperature for a given lattice configuration is obtained via the second derivative of the partition function Z , or of the pressure, Eq. (2.1), respectively. The extrapolation to the continuum limit is done by obtaining values for different $T \propto 1/N_\tau$ [34].

The order of the phase transition or existence of a smooth crossover at the transition from hadronic to partonic matter is obtained via the volume dependent behavior of the second derivatives of the partition function Eq. (2.3) at T_c .

In the chiral limit, $m_{u,d} = m_s = 0$, as well as in the opposite limit of the $SU(3)$, $m_{u,d} = m_s = \infty$, the phase transition is of first order. Nevertheless all current results state that the transition to the high temperature regime is not a real phase transition but a continuous crossover for physical quark masses and chemical potential $\mu \approx 0$ as at RHIC and LHC.

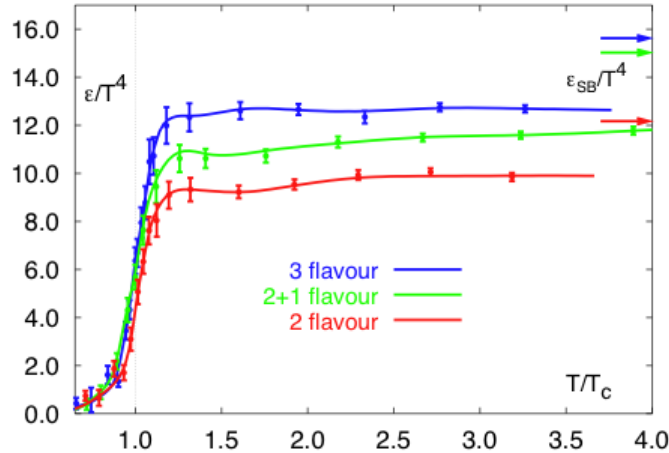


Figure 2.3.: The energy density ϵ in QCD. The Arrows indicate the ideal gas values ϵ_{SB} . This figure has been taken from [32].

2.2. Heavy Quark Potential

The QCD potential between two quarks is strictly confining in the pure gauge limit, $m_q \rightarrow \infty$, and for temperatures below T_c . It is commonly described with the Cornell-potential:

$$V(r) = -\frac{\alpha}{r} + \sigma r \quad (2.6)$$

Where r is the distance between the quarks under consideration, $\alpha = \alpha_s = \alpha_{QCD} \simeq 0.4$ the coupling constant in strong interactions and $\sigma \simeq 0.2 \text{ GeV}^2$ the string tension. The term proportional to $1/r$ describes analogous to the electromagnetic a potential a attractive force while the “additional” linear term, rises from the gluon self interacting property of QCD reflecting the string tension between quarks.

Figure 2.4 shows the behaviour of the quark anti-quark potential, the heavy quark free energy, respectively, for different temperatures from 0.82 to 3.29 T/T_c as well as the Cornell potential (solid line). For low distances the free energy is almost temperature independent. At larger r , the free energy characteristic is dominated by the temperature dependence. The free energy starts to deviate from the QCD potential at distances $r \approx 0.35 \text{ fm}$ for $T/T_c \approx 1$ and reaches a plateau at $r \approx 0.6 \text{ fm}$ due to strong screening effects.

The temperature effect on mesons depends hence on their binding radius. Mesons with rather low binding radii as the J/ψ meson survive the formation of a QGP plasma up to a temperature of 1.2 T/T_c as recent calculations [35] confirm. Excited states as the ψ' and mesons composed of lighter quarks are dissolved already at lower temperatures. A summary of recently calculated upper bounds on meson dissociation temperatures is given in Table 2.2.

A consequence of the J/ψ survival is that the statistical model as described in Chap. 1 is no longer valid as it is based on single quarks being able to propagate over substantial distances. The J/ψ yield influenced by the dissociation is also an indicator of the QGP temperature as indicated in Fig. 1.3.

Temperatures reached in SPS and RHIC are with $T \approx 1.3 T_c$ and $T \approx 2.1 T_c$ still high enough to melt J/ψ 's while Υ still survive RHIC energies. At LHC energies, corresponding to temperatures of $T > 3.5 T_c$ none of the particles listed in Table 2.2 survive the QGP.

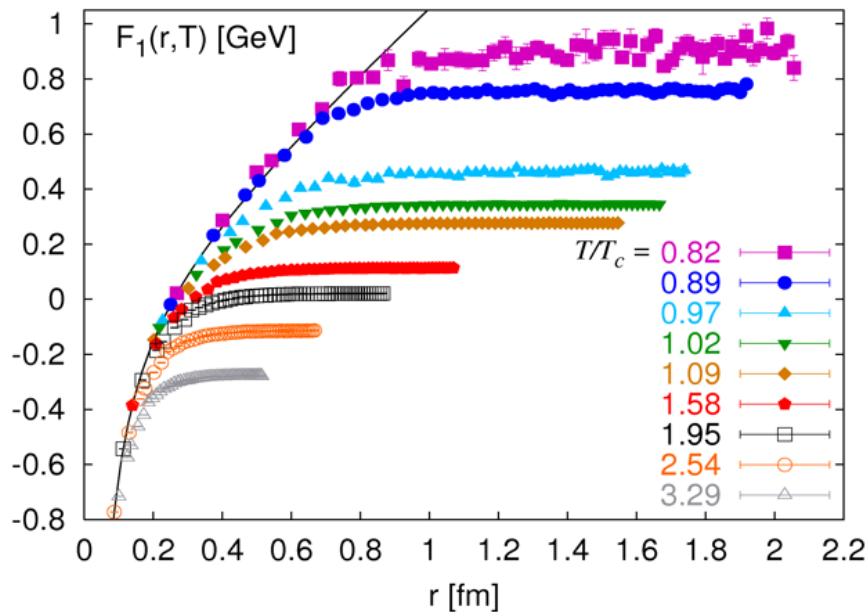


Figure 2.4.: The heavy quark free energy $F_1(r, T)$ versus the distance r between the quarks at various temperatures T/T_c and the zero temperature Cornell potential (solid band). The decrease of the linear slope with increasing temperature reflects the colour screening. This Figure has been taken from [25].

State	χ_c	ψ'	J/ψ	Υ'	χ_b	Υ
T_{dis}	$\leq T_c$	$\leq T_c$	$1.2 T_c$	$1.2 T_c$	$1.3 T_c$	$2 T_c$

Table 2.1.: Upper bound on dissociation temperatures. This table has been taken from [35]

2.3. The J/ψ meson

The discovery of J/ψ

In 1974 a resonance was found at a centre of mass energy of $3097 \text{ MeV}/c^2$. Its width of only 87 keV corresponding to a lifetime of about 10^{-20} s is extreme narrow thus long-living as compared to other mesons at the energy this resonance or particle was found. This new particle was named J/ψ . The existence of this resonance is explained by the creation of a heavy quark, which had not yet been discovered, although this *charm* quark (*c*-quark) has been postulated in 1970 by Glashow, Iliopoulos and Maiani.

The origin of the unique two-letter name is due to the fact that it was discovered almost simultaneously by two groups. One of the groups was located at the Brookhaven National Laboratory (BNL) and worked with the alternating gradient synchrotron (AGS) and colliding protons on a beryllium target. They named it “J” [36] which is one letter removed from “K” the name of an already known strange meson. On the other hand this name might be directly related to Samuel Ting’s name who headed the Massachusetts Institute of Technology (MIT) working group since the latin “J” strongly resembles the ideogram of Ting’s name written in Chinese.

The other group at the Stanford Linear Accelerator Center (SLAC) which collided e^+e^- at the Stanford Positron Electron Accelerating Ring (SPEAR) called it ψ [37]. Coincidentally the observed reconstructed track of a $\psi(3700)$ (exited J/ψ state, see below) decay looks like a ψ or fork (Fig. 2.5) in a spark chamber.

The decays that lead to the J/ψ discovery are:

$$\text{SLAC:} \quad e^+e^- \rightarrow \psi \rightarrow \text{hadrons} \quad (2.7)$$

$$\psi \rightarrow e^+e^-, \mu^+\mu^- \quad (2.8)$$

$$\text{BNL:} \quad p + \text{Be} \rightarrow \psi/J + \text{anything} \quad (2.9)$$

$$\psi \rightarrow e^+e^- \quad (2.10)$$

where the leptons (e^\pm, μ^\pm) are detected.

J/ψ as the lowest $c\bar{c}$ state has the photon-like quantum numbers $J^P = 1^-$. Where $J = S + L$ is the total angular momentum consisting of the spin $S = 1$ the angular momentum $L = 0$ and parity $P = +1$ indicating that the $c\bar{c}$ state is symmetric under parity transformation.

Generally a bound $c\bar{c}$ system is called *Charmonium* in analogy to the Positronium. Further more, the analogy to a hydrogen atom with an electron orbiting a proton gives an impression of a $c\bar{c}$ system. Nevertheless the main quantum number in a charmonium is defined differently than for an atom. The atomic convention for the main quantum number is $n_{Atom} = N + l + 1$, while for the charmonium $n_{q\bar{q}} = N + 1$ is chosen where N is the amount of “knots” of the radial wave function. This means

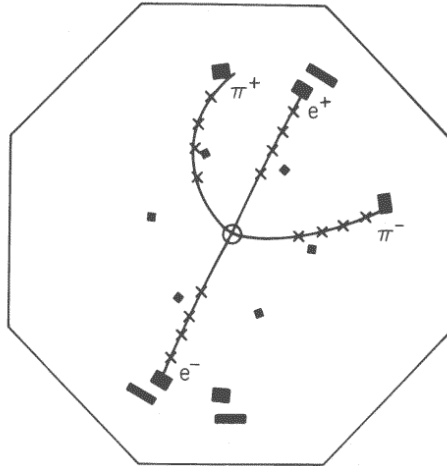


Figure 2.5.: Example of the decay $\psi(3700) \rightarrow \psi(3100) + \pi^+ + \pi^-$ observed in a spark chamber detector. The $\psi(3100)$ decays into $e^+ + e^-$ with about 1.5 GeV total energy while the pions have a relative low energy of 150 MeV . The magnetic field and SPEAR beam pipe are normal to the plane of the figure. The trajectory shown for each particle is the best fit through the sparks, indicated by crosses. This picture has been taken from [38].

e.g. the $2P$ state in the atomic nomenclature is called $1P$ for a charmonium. The quantum numbers for the J/ψ are then completed to $n^{2S+1}L_J = 1^3S_1$. For a naive hydrogen atom the Bohr radius [39] is:

$$r_0 = \frac{\hbar}{\mu c \alpha} \quad (2.11)$$

and the energy eigenstates,

$$E_n = -\frac{1}{2} \frac{1}{n^2} \mu c^2 Z^2 \alpha^2 \quad (2.12)$$

With the reduced mass $\mu = \frac{m_1 m_2}{m_1 + m_2}$. The obtained numerical values for a hydrogen atom are $r_0 \approx 5.3 \cdot 10^4 \text{ fm}$ and $E_n \approx -13.6/n^2 \text{ eV}$. The reduced mass of a hydrogen atom $\mu_H \approx m_e \approx 0.5 \text{ MeV}/c^2$ is about 3 orders of magnitude smaller than the one of the J/ψ meson $\mu_{J/\psi} = m_c/2 \approx 625 \text{ MeV}/c^2$ while the strong coupling α_s is about 2 orders of magnitude larger than the electro-magnetic one α_e . With this approach the J/ψ radius is $r_{J/\psi} \approx 1.5 \text{ fm}$ with $\alpha_s = 0.2$.

Less idealistic calculation with the Non-Relativistic Potential Theory using the Cornell potential Eq. (2.6) lead to a J/ψ radius of $r_0 \simeq 0.44 \text{ fm}$ [40].

Decay Channels of J/ψ

The J/ψ meson's lifetime being much longer than expected for a strongly decaying particle is explained by the OZI rule after Okubo, Zweig and Iizuka: Processes

with non-continuous quark lines in their Feynman graphs are suppressed. Thus, the favoured decay channel of a J/ψ meson is the one into two mesons which contain each a c (\bar{c}) quark as well as a light quark (u, d). However, this decay channel is energetically not possible since the masses of the later found D -mesons ($c\bar{u}, c\bar{d}\dots$) are with $m_{D^\pm} \approx 1870 \text{ MeV}/c^2$ [41] bigger than half of the J/ψ mass.

Since the decay channel of the J/ψ into to open charm mesons is forbidden, there are in principle two ways for a J/ψ to decay.

1. Foremost there is the annihilation of the quark and anti-quark into a virtual photon or gluon(s).

$$\begin{aligned} J/\psi (1^3S_1) &\rightarrow ggg \rightarrow \text{hadrons} \\ J/\psi (1^3S_1) &\rightarrow \text{virtual } \gamma \rightarrow \text{hadrons} \\ J/\psi (1^3S_1) &\rightarrow \text{virtual } \gamma \rightarrow \text{leptons} \end{aligned}$$

The J/ψ decay occurs electro-magnetically at a branching ratio of $\sim 25.4\%$ and results in hadrons or charged leptons. About 67.7% of the time the decay occurs via strong interaction.

Because at least two gluons are needed to form a colourless intermediate state and because of parity conservation, an odd number of gluons is required, only the strong decay via an intermediate state with *three* gluons is possible. Hence, a factor of α_s^3 enters in the decay probability. On the other hand, the electromagnetic decay takes place over only one virtual photon resulting in the electro-magnetic decay carrying a significant branching ratio. The branching ratio of $J/\psi \rightarrow e^+e^-$ as well as $J/\psi \rightarrow \mu^+\mu^-$ is 5.9% .

2. The other possible decay is the weak decay of one or both heavy quarks, e.g.

$$J/\psi \rightarrow D_s^- + e^+ + \nu_e$$

The weak decays are negligible with a branching ratio of $\sim 10^{-5}$ [41].

For center of mass energies higher than 3.1 GeV even more resonances are found and identified as excited states of the $c\bar{c}$ system. The first excited state with $m = 3.686 \text{ GeV}/c^2$ is called ψ' or in the spectroscopic nomenclature $\psi(2S)$ followed by e.g. $\psi(3770) \equiv \psi(3S)$ up to $\psi(5S)$ with a mass of 4415 MeV .

Since ψ' is still below the mass boundary of twice the D -meson mass its decay width is with 337 keV also rather small. The term scheme of the charmonium system is shown in Fig. 2.6. As is illustrated, a slightly lower $c\bar{c}$ state than the J/ψ called η_c exists with $J^P = 0^-$.

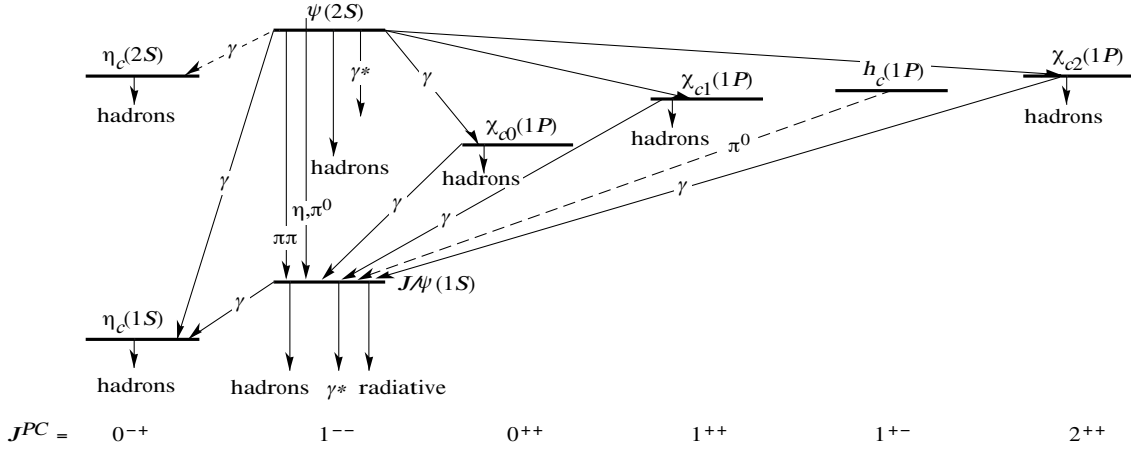


Figure 2.6.: Term scheme of the J/ψ family. This figure has been taken from [41].

The Analysed Decay Channel

The focus of detecting J/ψ 's is on the decay into two leptons, namely into e^+e^- or $\mu^+\mu^-$. As described in Chap. 3 in the ALICE experiment the muon-arm is build to detect muons and one of the main goals of the central barrel, especially the TRD sub-detector is to identify electrons and reconstruct their paths through the detectors as described in Chap.4 and Chap.5. Since outstanding results are expected from the TRD and the large hadronic background the channel

$$J/\psi \rightarrow e^+ + e^-$$

is the one examined in the following.

3. LHC and ALICE

3.1. The Large Hadron Collider

The Large Hadron Collider (LHC) is located at the European Organisation for Nuclear Research (Conseil Européen pour la Recherche Nucléaire, CERN) near Geneva, Switzerland. The first circulating beam was seen at 10. September 2008. First collisions are expected to take place in spring 2009. At its full capacity two counter rotating beams of protons or heavy ions are brought to collision at an unprecedented high center of mass energy and luminosity. Due to this enormous collision energies new insights into the structure of matter and fundamental forces will be possible. The design center of mass energy of $\sqrt{s} = 14$ TeV in $p+p$ collisions at a luminosity of $\mathcal{L} = 10^{34} \text{ cm}^{-2}\text{s}^{-1}$ [42] will exceed the up-to-date highest available energies of the Tevatron by a factor of 7 and the luminosity by a factor of 100. In lead-lead collisions the center of mass energy of 5.5 TeV per nucleon-nucleon pair which will be reached is higher by a factor of 30 than compared to the collision energies of the Relativistic Heavy Ion Collider (RHIC) at the Brookhaven National Laboratory (BNL). The nominal luminosity in lead-lead collisions in LHC is $\mathcal{L} \approx 10^{27} \text{ cm}^{-2}\text{s}^{-1}$. The LHC was constructed inside the existing tunnel of the Large Electron Positron (LEP) collider which stopped its operation on 2000. A schematic overview of the CERN accelerator system is shown in Fig. 3.1.

Protons from a 90 kV duoplasmatron proton-source are accelerated in the linear accelerator LINAC2 to a kinetic energy of 50 MeV and then passed to the multi ring Proton Synchrotron Booster (PSB) where they are accelerated to 1.4 GeV. In the Proton Synchrotron (PS) they reach 26 GeV and their bunch patterns are generated. After the transfer to the Super Proton Synchrotron (SPS) protons are accelerated to 450 GeV and injected into the LHC ring with about 27 km circumference where they reach 7.5 TeV. To keep the protons along the ring, 1232 superconducting dipole magnets are installed. They are cooled down to 1.9 K by liquid helium and provide a magnetic field up to 8.3 T. Additionally, 392 quadrupole magnets keep the beams focused.

Lead ions from an electron cyclotron resonance source are bunched and accelerated by a radio frequency quadrupole. They are selected in the charge state Pb^{27+} and further accelerated in the linear accelerator LINAC3 to 4.2 MeV/nucleon. After that, they are stripped by a carbon foil and the charge state Pb^{54+} is selected in a filter line. These selected ions are further accelerated in the low energy ion ring (LEIR)

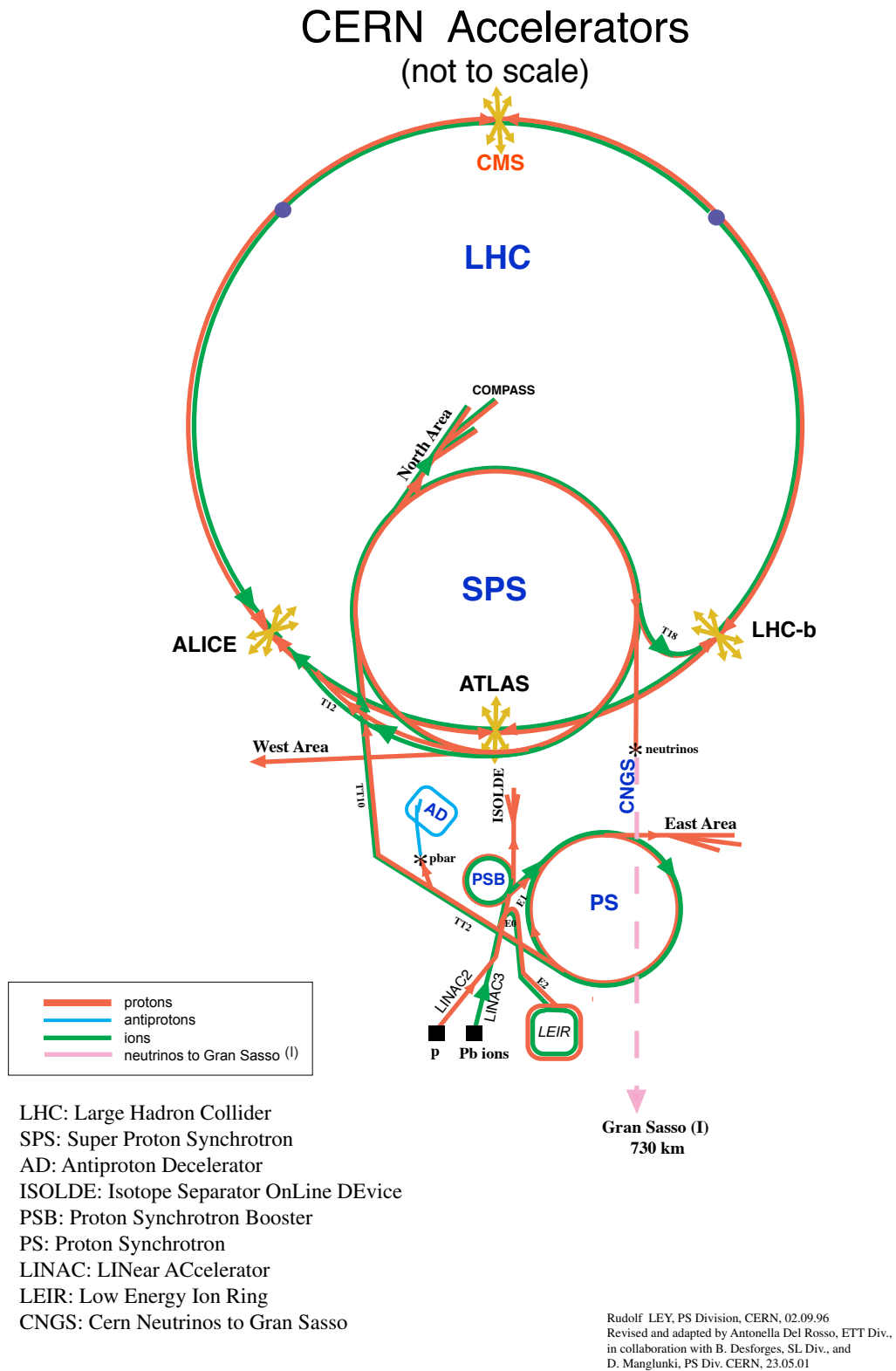


Figure 3.1.: Overview of the accelerator system at CERN. This figure has been taken from [43].

to an energy of 72 MeV/nucleon . From there the ions are transferred to the PS where they are accelerated to 5.9 GeV/nucleon and sent to the SPS. In between they pass another foil which fully strips the ions to Pb^{82+} . The SPS accelerates the fully stripped ions to 177 GeV/nucleon , before injecting them into the LHC where they reach a maximum energy of 2.76 TeV/nucleon .

The two beams are brought to collision at eight interaction points. At four of the interaction points the main experiments are located as indicated in Fig. 3.2.

ATLAS: The main goal of A Toroidal LHC Apparatus (ATLAS) experiment is the discovery of the Higgs-Boson and the investigation of theories beyond the standard model, i.e. the search for supersymmetric particles and extra dimensions.

CMS: The Compact Muon Solenoid (CMS) is designed to analyze the nature of matter. In principle the CMS and the ATLAS experiments are built for the same purpose applying complement detector technologies.

LHCb: The LHC Beauty (LHCb) experiment is built to observe CP violation in B-meson systems. The results are dedicated to understand the difference between matter and antimatter within the universe.

ALICE: A Large Ion Collider Experiment (ALICE) is the dedicated heavy ion detector at the LHC. The ALICE detector is designed to identify and characterize the quark gluon plasma. ALICE is briefly described in the next section.

3. LHC and ALICE

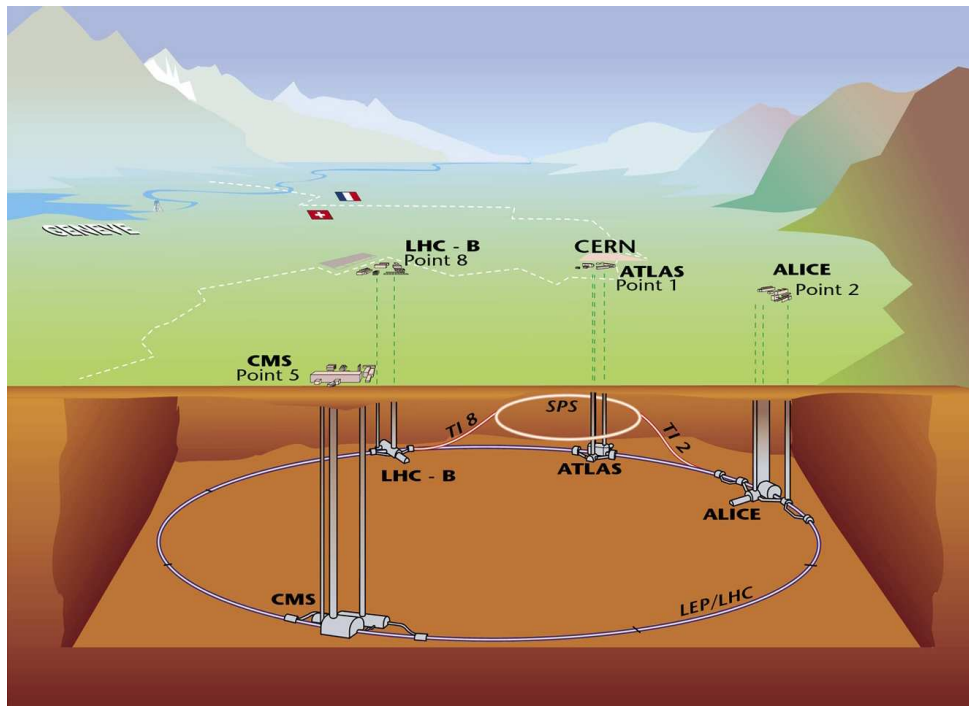


Figure 3.2.: Schematic view of the Large Hadron Collider and its four experiments ALICE, ATLAS, LHCb and CMS. This figure has been taken from [43].

3.2. A Large Ion Collider Experiment

A Large Ion Collider Experiment (ALICE) is designed to determine the identity and precise trajectory of more than ten thousand charged particles over a large momentum range from 100 MeV/ c to 100 GeV/ c in transverse momentum. The layout of the ALICE detector which is split into the so-called Central Barrel and the Muon arm is illustrated in Fig. 3.3.

The Muon Arm covering a pseudo-rapidity range from $-2.4 < \eta < -4.0$ is dedicated to the measurement of muons. Hadrons and electrons are removed by the absorber made predominantly out of carbon and concrete. The muon tracks are bent for momentum measurement by the dipole magnet with an integrated field of 3 Tm and then detected by the tracking system which covers a total area of about 100 m² and achieves a spatial resolution of about 100 μ m. The tracking system consists of cathode pad chambers which are arranged in five stations: two are placed before, one inside and two after the dipole magnet. The stations are made of two chamber planes. Their size ranges from few square metres for the first station to more than 30 m² for last station. To trigger on J/ψ or Υ a trigger system, arranged in two stations placed behind the muon filter consisting of four Resistive-Plate Chamber (RPC) planes with the total active area of about 150 m², is used.

The ALICE central barrel covers the kinematic region around mid-rapidity $|\eta| < 0.9$ and is surrounded by the L3 solenoidal magnet which produces a homogeneous magnetic field of up to 0.5 Tesla parallel to the beam axis. This magnetic field provides momentum dispersion for charged particles in the plane transverse to the beam axis.

The central part of ALICE is an assembly of various detectors. The detectors providing information like momentum, vertex coordinates and particle identification are the Inner Tracking System (ITS), the Time Projection Chamber (TPC), the Transition Radiation Detector (TRD) and the Time of Flight detector (TOF). They all cover a pseudo-rapidity range of $|\eta| < 0.9$, full azimuth and comprise the ALICE central barrel. The central barrel is used for the presented studies and is described in more detail in the following.

Inner Tracking System

The main purpose of the Inner Tracking System (ITS) is the determination of vertices with high spatial resolution. Additionally the ITS provides tracking and identification of particles with momenta down to 100 MeV/ c and improves the momentum resolution of tracks with higher momentum. To cope with the large number of charged particles expected to be produced in a lead-lead collision the ITS has a high granularity and radiation hardness. To keep the distortion of tracks of charged particles to a minimum, the total thickness of ITS was optimised to be 7% radiation length. Therefore the ITS consists of six cylindrical layers each of a different type: the first two layers are Silicon Pixel Detectors (SPD), followed by two layers of Silicon Drift Detectors (SDD)

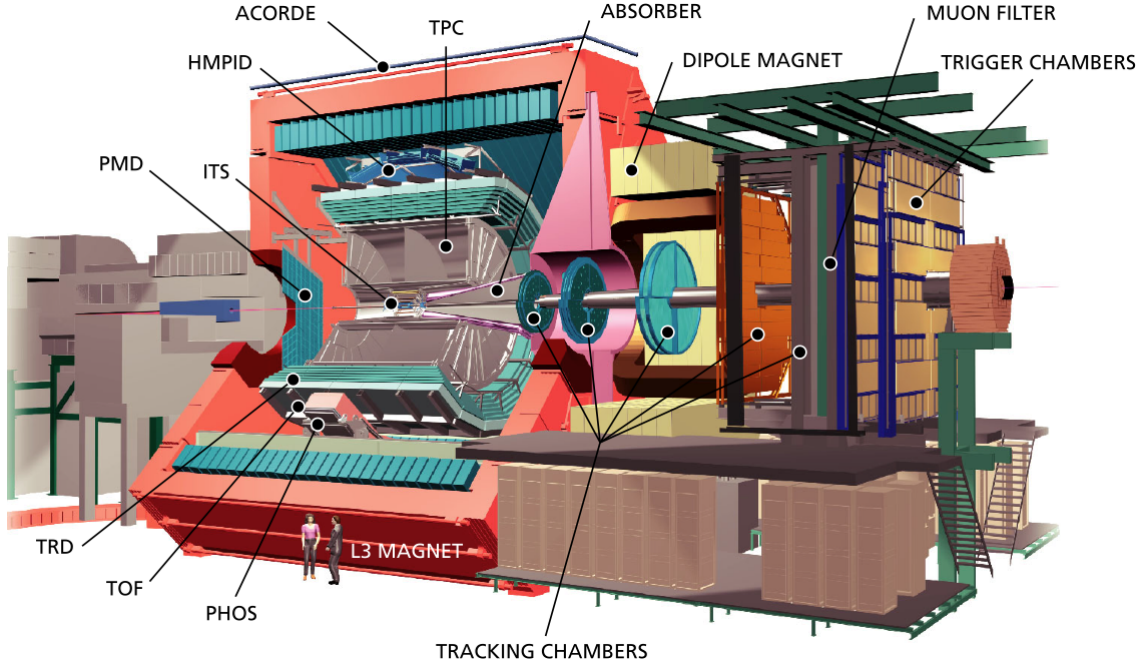


Figure 3.3.: Schematic layout of the ALICE detector. This figure has been taken from [44].

and two layers of double-sided Silicon micro-Strip Detectors (SSD). These six layers are located at radii $r = 4, 7, 15, 24, 39$ and 44 cm [44]. The first layer is located only 4 cm away from the beam axis, and covers almost four units of pseudo-rapidity. The two layers of SPD have a spatial resolution of $12 \mu\text{m}$ in the $r\phi$ -plane and $70 \mu\text{m}$ in z -direction, the resolution of the two layers of SDD is $28 \mu\text{m}$ in z -direction and $38 \mu\text{m}$ in $r\phi$ -direction while the two outer layers have a $20 \mu\text{m}$ $r\phi$ -resolution and $830 \mu\text{m}$ z -resolution. The precise measurement in ITS allows the extrapolation of tracks back to the primary vertex of the collision with an impact parameter resolution better than $100 \mu\text{m}$.

Time Projection Chamber

The Time Projection Chamber (TPC) is the main tracking detector in the central barrel ($|\eta| < 0.9$) of the ALICE experiment. The TPC provides charged particle momentum measurement and primary vertex determination with precise momentum resolution at a large tracking efficiency of 90% and two-track separation up to a p_T region of more than $10 \text{ GeV}/c$. Additionally correct pattern recognition of the high multiplicity Pb+Pb central collisions at the LHC energy are achieved by the TPC. Up to 20 thousand primary and secondary charged tracks per event are expected in the sensitive volume. The cylindrical TPC has an inner radius of 80 cm, an outer radius of 250 cm and an overall length of 5 m, covering full azimuth. This means the ALICE TPC is with its active volume of about 95 m^3 the largest TPC ever built. The total material budget is kept at the level of 3% radiation length to ensure minimal

multiple scattering and secondary particle production. The TPC cylindrical field cage of 88 m^3 size is divided by a central electrode into two drift regions. The high voltage central electrode provides a uniform electrostatic field of 400 V/cm . The whole drift volume in the cage is filled with a gas mixture of 85% Ne / 10% CO₂ / 5% N. Within this drift gas the maximum drift time is $t \sim 88 \mu\text{s}$. Three-dimensional space points are reconstructed from the measured drift time (z-direction) and the position on the cathode pads (x, y-direction) of the induced signal. In total, the TPC provides up to 160 space points for each particle trajectory. Additionally the TPC contributes strongly to the particle identification. Particles are identified within the TPC by their specific loss of energy due to interactions with the TPC gas. More details are discussed in the next chapter.

Transition Radiation Detector

The Transition Radiation Detector (TRD) identifies electrons with $p_T > 1 \text{ GeV}/c$ and provides fast trigger capability of $6 \mu\text{s}$. More details of the TRD are described in Chap. 4.

Time Of Flight

The Time Of Flight (TOF) detector is the most outer part of the ALICE tracking chain and extends the identification of hadrons, namely π , K , p , in a momentum range up to $4 \text{ GeV}/c$ by measuring the time a particle needs to fly from the interaction point to a radial distance of approximately 4 m. TOF is composed of 18 supermodules surrounding the 18 TRD supermodules and covers a surface larger than 160 m^2 . The TOF detector is composed of multigap resistive plate chambers (MRPC) which achieve a time resolution of 65 ps at a rate of more than $50 \text{ Hz}/\text{cm}^2$.

The detectors dedicated to a specific physics task are the Photon Spectrometer (PHOS) measuring high momentum photons, the High Momentum Particle Identification (HMPID) to separate kaons from pions and protons and the Electro-magnetic Calorimeter (EMCAL) for the detection of high momentum electro-magnetic probes. These three detectors cover only a small part of the full acceptance. A detailed description of the individual subcomponents of ALICE is found in [45].

ALICE Coordinate System

The *global* coordinate system is defined in accordance with the LHC. The origin is defined as the arbitrary center of the detector where the collision ideally occurs. The z -axis is parallel to the beam direction. Perpendicular to the z -axis is the transverse $r\phi$ -plane in x, y -direction, where the x -axis is horizontal, and the y -axis is vertical. The system is right-handed, with positive x pointing inwards referred to the LHC ring, positive y pointing upwards and positive z pointing in the opposite direction of the muon arm. The azimuthal angle Φ increases, starting in x -direction $\Phi = 0^\circ$ counter-clockwise viewed

from z -direction. This coordinate system is generally used to locate an object described in the global view of the detector, e.g. the sub-detectors, the track vertex, etc.

Clusters and tracks are always expressed in a *local* coordinate system related to a given sub-detector (TPC super module, ITS module etc). This local coordinate system is defined as following:

- it is a right handed-Cartesian coordinate system;
- its origin and the z axis coincide with those of the global ALICE coordinate system;
- the x axis is perpendicular to the sub-detector's sensitive plane e.g. the TPC pad row, ITS ladder, TRD pad plane.

This choice reflects the symmetry of the ALICE setup and therefore simplifies the reconstruction equations. It also enables the fastest possible transformations from a local coordinate system to the global one and back again, since these transformations become single rotations around the z -axis.

4. The Transition Radiation Detector

4.1. Energy Loss of Charged Particles

A charged particle deposits energy if it traverses matter, e.g. if it passes through the drift chambers gas of the TRD. Processes of energy loss by ionisation are described by the *Bethe-Bloch formular*. Radiative energy loss or *Bremsstrahlung* and transition radiation are further processes of energy loss. These processes depend on the particle velocity. Thus, at a given momentum it allows for the determination of its mass and hence the particle's identity.

Ionisation and the Bethe-Bloch Formula

When passing through a medium a charged particle loses energy via ionisation or excitation of the constituent atoms. The mean energy loss per path length is derived from the Rutherford formula for elastic scattering and is described by the *Bethe-Bloch formula* [38]:

$$-\frac{dE}{dx} = \frac{4\pi N_A z^2 e^4 Z}{mv^2 A} \left[\ln \left(\frac{2mv^2}{I(1-\beta^2)} \right) - \beta^2 \right] \quad (4.1)$$

The path length x in the medium is usually given in [$g\text{ cm}^{-2}$ or $kg\text{ m}^{-2}$] and corresponds to the amount of matter traversed. Here, m is the electron mass, z and v are the charge and velocity of the traversing particle. The relativistic velocity is given by $\beta = v/c$, N_A is Avogadro's number and I is an effective ionisation potential of the atom species of the medium, averaged over all electrons, with approximate magnitude $I = 10 Z\text{ eV}$ [38]. Z and A are the atomic number and mass number of the medium's atoms. The energy loss described by Eq. (4.1) drops with $1/\beta^2$ for small $\gamma = E/Mc^2 = (1-\beta^2)^{-1/2}$, M being the mass of the passing particle, reaches a minimum for $E \simeq 3 Mc^2$ and increases afterwards logarithmically with γ . The drop is due to the particle having less time to interact with the medium the faster it gets. The slow rise for high γ originates from relativistic effects, leading to an increase of the transverse electric field of the particle which enables atoms of the medium that are further away from the particle's path to interact with the particle.

This effect saturates into the Fermi plateau, since the polarisation of the medium shields the electro-magnetic field of the moving particle.

The energy loss described by Eq. (4.1) is independent of the particle mass M . The specific energy loss of different particles with the same momentum $p = Mv$ is used to identify the particle species if momentum of the particle is known, e.g. via the curvature of the path in the magnetic field.

Bremsstrahlung

Additionally to ionisation, particles loose energy due to radiation of photons when traversing matter. The electric field of the atomic nuclei of the medium decelerates the passing particle, resulting in the emission of a photon, therefore the name *Bremsstrahlung*.

The average energy loss per unit length is given by:

$$-\frac{dE}{dx} = 4\alpha_e N_A \frac{Z^2}{A} z^2 r_0^2 E \ln \frac{183}{Z^{1/3}} \quad (4.2)$$

$$-\frac{dE}{dx} = \frac{E}{X_0} \quad (4.3)$$

With variables and constants as in Eq. (4.1) and , the classical electron radius $r_0 = \hbar/c\alpha_e M$, M donating the electron mass. Energy loss from Bremsstrahlung drops with the traversing particle's mass squared M^{-2} and rises proportional to its energy E . Therefore Bremsstrahlung is mainly seen from electrons. X_0 is the characteristic radiation length after which the energy of the particle is reduced by a factor $1/e \approx 1/3$.

For low energies the energy loss is dominated by ionisation. However the ionisation effect is almost constant for high energies, while the radiative energy loss rises with E Bremsstrahlung becomes the dominating effect. For electrons the critical energy at which both effects contribute equally is:

$$E_c \simeq \frac{600}{Z} \text{ MeV}. \quad (4.4)$$

Transition Radiation

Another radiative effect is transition radiation (TR). It is produced if an ultra-relativistic particle crosses the boundary surface of two media with different dielectric constants, fraction indices n , respectively. The electro-magnetic field of a charged particle changes with the dielectric constants of the medium by which it is surrounded. Since the electric field is continuous at the boundary region the field

of the charged particle has to change, hence radiation is emitted. A qualitative description of transition radiation is obtained from classical electro dynamics by using the model of a mirror charge of the particle within the medium with opposite charge and equal distance to the boundary surface. The actual particle and its mirror self form a dipole evolving in time since the particle is moving towards the boundary and so is its mirror charge. Therefore radiation is emitted in an angle of $\Theta \propto 1/\gamma$. The typical energy of an emitted photon is $E_\gamma \simeq \gamma \hbar \omega_p$ with the plasma frequency of the corresponding medium $\omega_p = \sqrt{4\pi\alpha n_e/m_e c^2} = 28.8 \sqrt{\rho \frac{Z}{A}}$.

Since the transition radiation is related to $\gamma = \sqrt{1/1 - \beta^2}$ whereas other energy loss effects depend on β , transition radiation is a great tool to identify particles in higher momenta regions. For the momenta at which particles reach the TRD, electrons are the only particles with $\gamma > 1000$ and therefore produce transition radiation making TR a good tool to identify electrons.

On the other hand, the mean number of emitted transition radiation photons per boundary surface is with about $\frac{1}{137} = \alpha_e$ rather low. Within a TR detector many boundary surfaces are therefore used, realised as foil sequences, micro fibers or other materials providing a large number of boundary surfaces. The number of TR photons is, though, limited and saturates for many boundary surfaces, because of interference effects. For regular foil sequences analytic calculations are possible which are not possible for other radiator types.

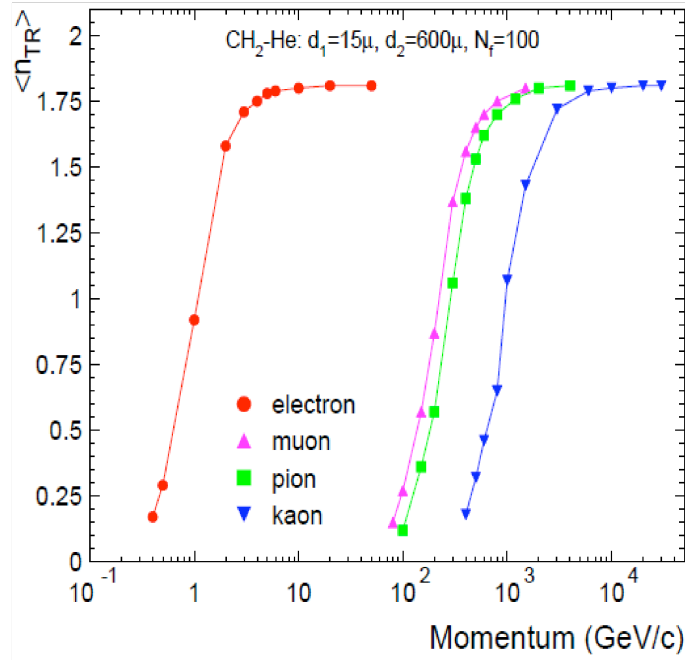


Figure 4.1.: The mean number of transition radiation photons produced by various particles versus momentum. The mean number rises and saturates quickly after a threshold momentum is reached.

4.2. Detector Design

The ALICE TRD is located between the TPC and the TOF in the radial range from 2.9 m to 3.7 m in the ALICE spaceframe with an overall length of 7 m. It consists of 540 gas detector modules arranged in 18 supermodules mounted in radial direction. Each supermodule is divided into 6 layers in radial direction and 5 stacks in beam direction. Hence one supermodule consists of 30 detector modules.

Part of each of the 540 modules is a sandwich radiator and a multiwire proportional chamber, whose drift region filled with 85% Xe and 15% CO₂. The multiwire proportional chamber includes the drift region and the amplification region. The drift region has a width of 3 cm and the amplification region as another part of the module 0.7 cm.

In the sandwich radiator as many boundary surfaces as possible are used to reach a higher yield of transition radiation. Nevertheless, stacks of foils do not provide sufficient mechanical stability and additional supply structures would be needed to strain the foils. The supply structures would lead to large inactive areas which not only reduce the acceptance of the TRD but also spoil the possible results of detectors behind the TRD. The solution found for the ALICE TRD radiator is a combination of foam and fibres providing the optimal combination of TR efficiency and mechanical stability. Figure 4.2 shows the principle design of the radiator sandwich. The supporting structure with good transition radiation production rate is made out of a polymethacrylimide foam, called Rohacell HF71 of 8 mm thickness reinforced by glass fibre sheets. The inner volume of the sandwich cells is filled with polypropylene fibre mats being the main radiator material. Scanning electron microscope images of both materials are shown in Fig. 4.3.

Since it is not possible to calculate the energy loss of such materials analytically, simulations of the detector response parametrisations are used. In the case of the ALICE TRD the behavior of the radiator is modeled by a foil stack in good agreement with measured results.

The design of the ALICE TRD as well as the signal creation is schematically shown in Fig. 4.4. The large cluster at the beginning of the drift chamber originates from a transition radiation photon of the electron. Electrons produced by ionisation energy loss (dE/dx) and by transition radiation absorption drift along the field lines toward the amplification region where they produce avalanches around the anode wires. These avalanches induce a signal on the cathode pads. The insert in the right figure shows the distribution of pulse height over pads and time bins spanning the drift region for a measured electron track. The local coordinate system shown is the coordinate frame of a single readout chamber with the z -direction parallel to the beam axis.

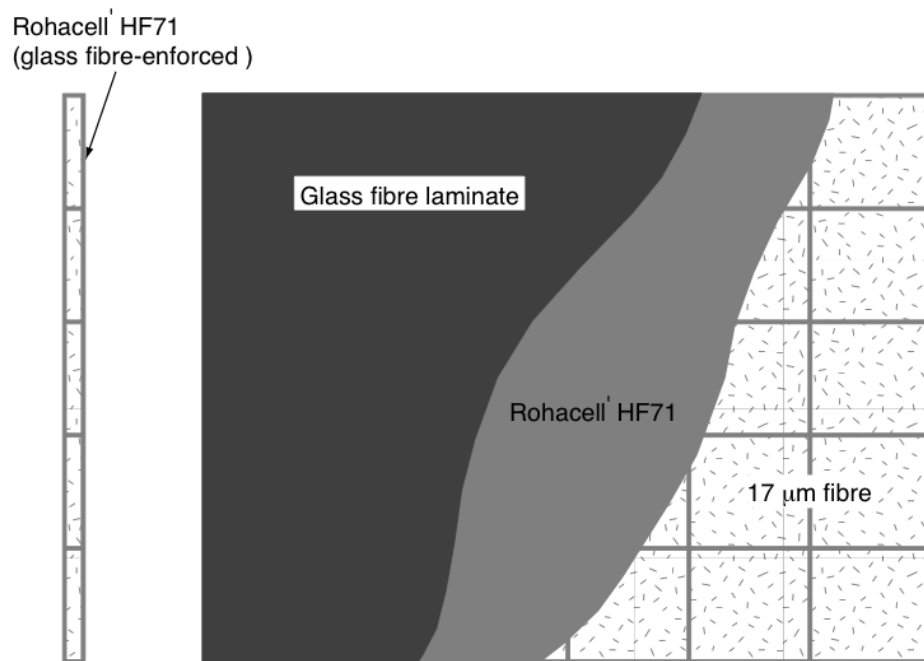


Figure 4.2.: Schematic design of a ALICE TRD sandwich radiator providing the optimal combination of TR efficiency and mechanical stability. This Figure has been taken from [45].

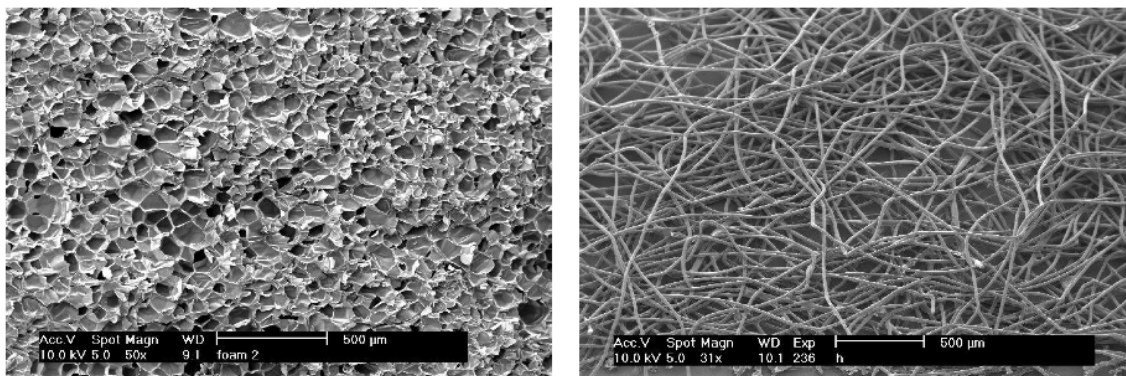


Figure 4.3.: Scanning electron microscope images of the used radiator materials: Rohacell HF71 foam (left) and fibres mat (right). This Figure has been taken from [45]

4. The Transition Radiation Detector

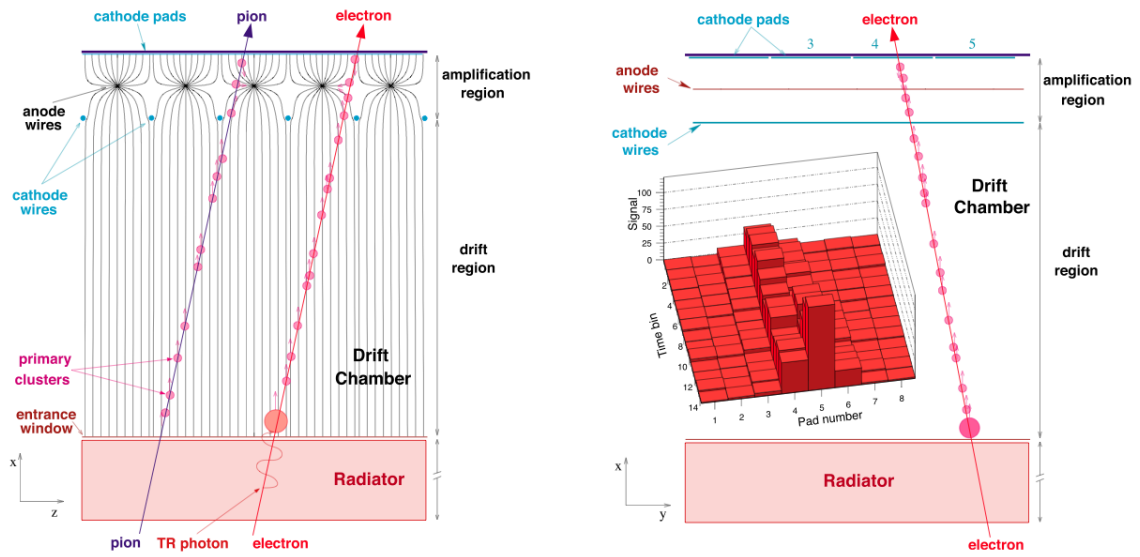


Figure 4.4.: The principle of the ALICE TRD. The left figure shows the projection in the plane perpendicular to the wires. The right figure shows the projection in the bending plane of the ALICE magnetic field. In this direction the cathode plane is segmented into the pads from 0.635 to 0.785 *cm* width. The insert shows the distribution of pulse height over pads and time bins spanning the drift region for a measured electron track. This Figure has been taken from [45].

4.3. Charged Particle Identification

The ALICE experiment identifies particles over a large range of momenta from about 0.1 GeV/ c up to a few tens of GeV/ c . This is achieved by combining the information obtained by the different sub-detectors, ITS, TPC, TRD, TOF and HMPID, which are optimised for smaller momentum ranges as illustrated in Fig. 4.5.

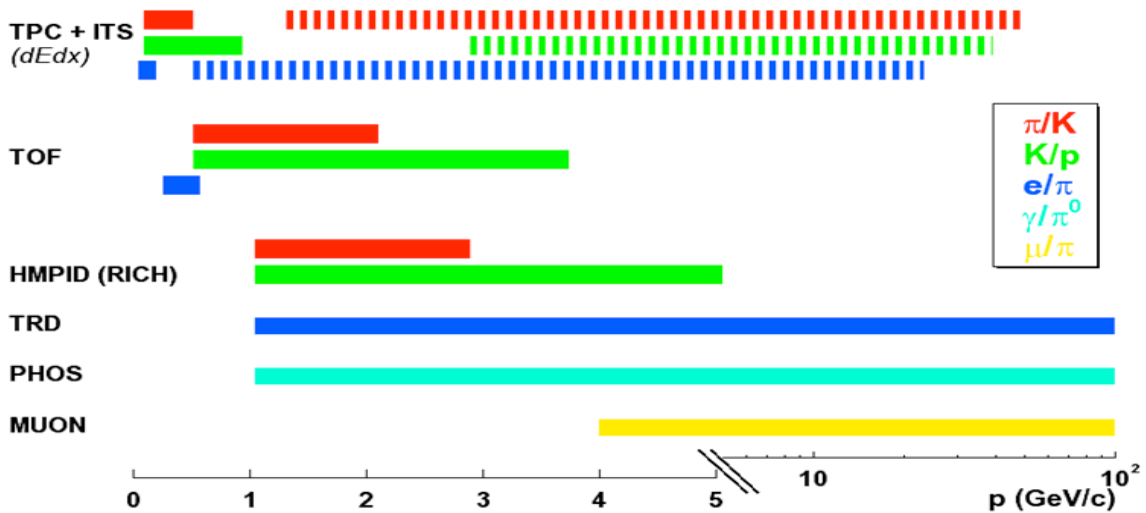


Figure 4.5.: Particle identification in ALICE: momentum range and detectors used. This Figure has been taken from [46]

First a brief overview of the particle identification (PID) methods and capabilities, e.g. found in [44] for the four main central barrel sub-detectors is given, followed by more detailed information about PID with the TRD.

- *ITS* uses energy loss in the non-relativistic ($1/\beta^2$) region, therefore particle identification of low momentum particles and reconstruction of secondary vertices is possible.
- *TPC*: Charged particles ionise the gas of the detector. The Bethe-Bloch equation Eq. (4.1) relates the velocity β of a particle to its mean energy loss per path length, dE/dx . The TPC is designed to provide dE/dx information with a resolution better than 7%. Combining dE/dx and momentum information yields the particle identity.
- *TRD* uses the production of transition radiation by electrons additional to ionisation energy loss. It is designed to detect electrons at higher transverse momenta $p_t > 1$ GeV/ c and helps substantially to improve the e/π separation, as discussed in more detail in the next section.

- *TOF* uses the time of flight a particle needs to traverse a defined path length. TOF is used for separating kaons and pions up to $p_T < 3 \text{ GeV}/c$ and kaons and protons up to $p_T < 5 \text{ GeV}/c$.

Each of the sub-detectors gives a standalone particle identification. When a track is reconstructed in more than one sub-detector simultaneously, the particle identification is improved by combining the single detector PID information.

Particle Identification with the TRD

Particles entering the TRD drift chamber, as well as transition radiation photons they produced, ionise the gas in the chamber and create electron clusters. The transition radiation photon is absorbed shortly after entering the drift chamber due to the chosen gas mixture. The primary particle constantly generates electron clusters on its way through the chamber.

The final signals produced at the cathode pads as described above are read out at a 10 MHz sampling rate such that the signal height on all pads is sampled in time bins of 100 ns . Figure. 4.6 shows the measured average signals of pions and electrons with and without transition radiation versus the drift time. For small drift times the average pulse height increases rather strongly, it is about twice as high as for time bins in the mid-region. This is due to the signal coming from the amplification region. The following plateau originates from the drift region. The signal from transition radiation of the electrons arrives preferentially later, in higher time bins, since the radiation photons are produced at the entrance of the detector and therefore any signal deriving from them has the longest distance to travel until it is read out.

In the following the main purpose of the TRD being the separation of electrons and pions is discussed.

However, the principle of identifying other particles like muons, kaons and protons is the same and look-up tables for each of them exist.

The first approach is the:

LQ-Method

For this *Likelihood* method the total deposited energy shown in Fig. 4.7, produced charge Q respectively, in one TRD layer is taken into account. Electrons and pions have the probability $P(E_n)$ to deposit the energy E_n in each layer. The total

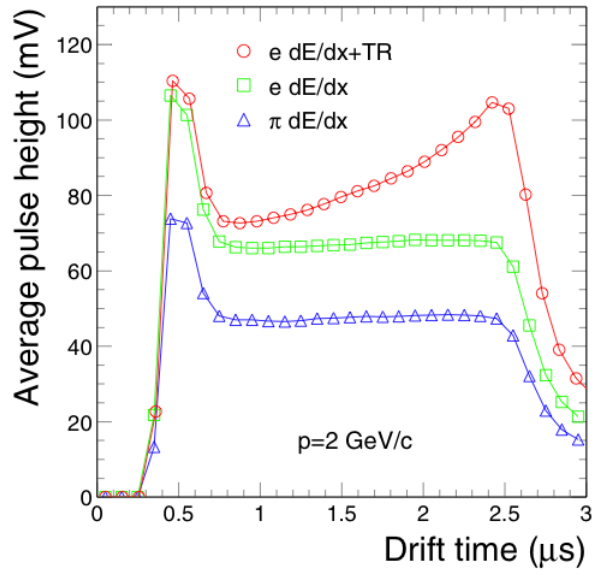


Figure 4.6.: Average pulse height versus drift time for electrons (upper and middle) and pions (lower). The different pulse heights indicate the different ionization energy (dE/dx) loss of electrons (green rectangles) and pions (blue triangles). The characteristic peak at larger drift times of the electron (red circles) is due to the absorbed transition radiation. This Figure has been taken from [45].

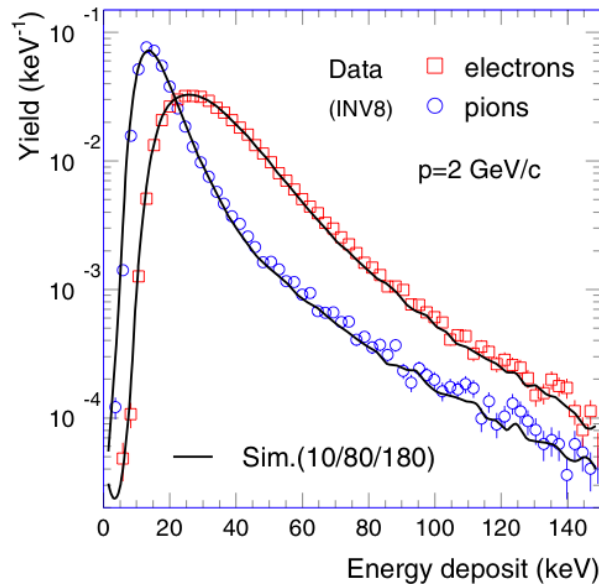


Figure 4.7.: Integrated energy deposit for pions and electrons for a momentum of $2 \text{ GeV}/c$. The symbols represent the measurements, the lines are calculations. This Figure has been taken from [47].

probability of an electron to produce a set of measured values is defined by:

$$P_e(E) = \prod_{n=1}^6 P^n(E_n|e) = \sum_{n=1}^6 P(E_n|e) \quad (4.5)$$

where the sum has to be taken over all $n = 6$ layer and the probability P is assumed to be the same in every layer. For pions the analog expression is:

$$P_\pi(E) = \prod_{n=1}^6 P(E_n|\pi) \quad (4.6)$$

The probability or likelihood that the energy E is deposited by an electron is hence given by:

$$L_e(E) = \frac{P_e(E)}{P_e(E) + P_\pi(E)} \quad (4.7)$$

This likelihood distribution is illustrated for 2 GeV/ c electrons and pions in Fig. 4.8. The purple band indicates the region to which 90% of all electrons belong and is taken as a baseline value. This is the definition of the *electron efficiency* meaning that 90% of all electrons are identified correctly. For 90% electron efficiency a pion efficiency of 1% or a pion suppression (factor) of 100 is achieved, meaning that only one out of 100 pions is misidentified as an electron.

Factors influencing the pion efficiency are:

1. The chosen electron efficiency. The pion efficiency improves substantially by almost an order of magnitude when lowering the electron efficiency from 0.9 to 0.7. Nevertheless, the improvement of the pion suppression does not compensate the loss of this amount of electrons since e.g. the quarkonia yield depends quadratically on the electron yield.
2. The number of layers ergo the amount of information available for the probability calculations. Not every track leaves useable PID information in each layer, because of the statistical character of energy loss and the geometric acceptance. The, with about a factor of two per layer, strong dependence of the pion efficiency on the number of layers used in the PID calculations is shown in Fig. 4.9 for fixed electron efficiency and particles with momentum $p = 2$ GeV/ c .
3. The momentum of the particle. The momentum dependence of the pion rejection is shown in Fig. 4.10. The data points (red) indicate that the pion efficiency increases from momenta larger than 2 GeV/ c on. At $p = 6$ GeV/ c the pion rejection is about a factor 2 worse than it is at 2 GeV/ c . In this regime, the transition radiation yield, which almost saturates, no longer compensates the relativistic rise of the pions deposited energy (dE/dx).

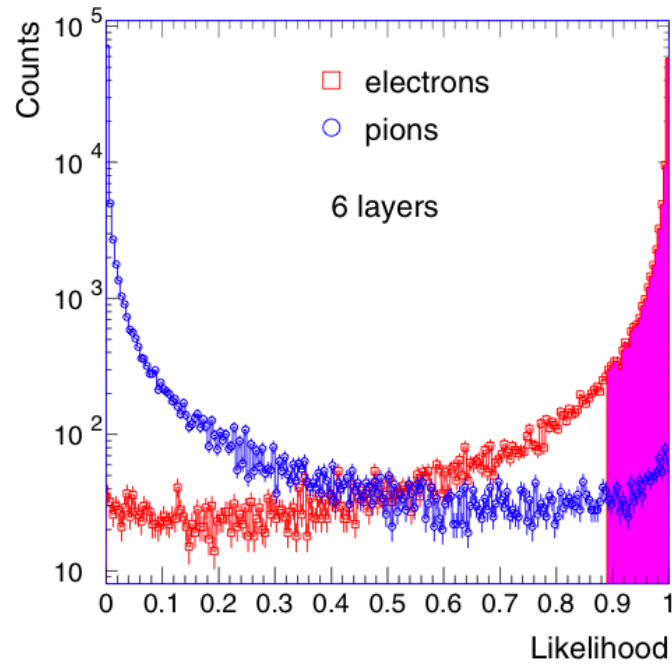


Figure 4.8.: Distributions of the likelihood (to be an electron) for electrons and pions of 2 GeV/c, obtained from the total energy deposit. The shaded area corresponds to 90% electron efficiency. This Figure has been taken from [47].

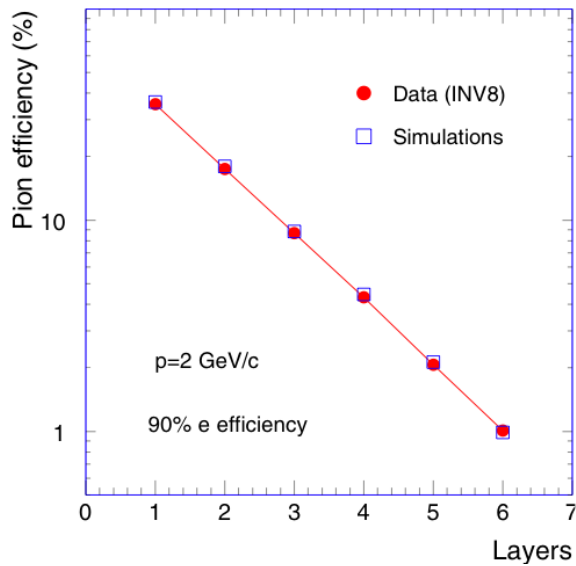


Figure 4.9.: Pion efficiency as a function of the number of layers for a momentum of 2 GeV/c. This Figure has been taken from [47].

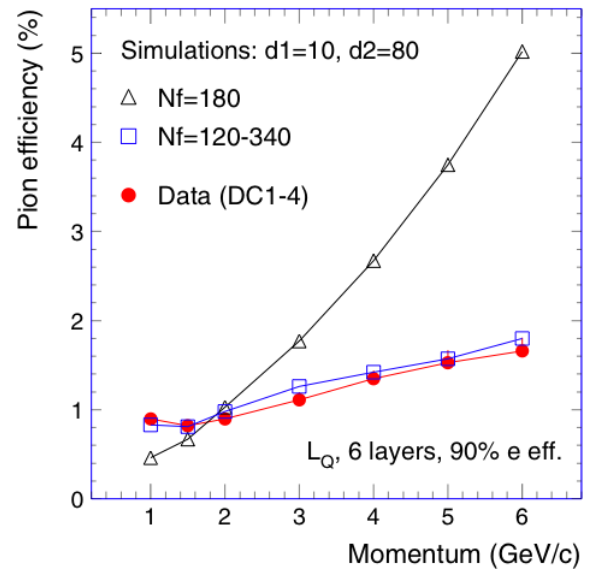


Figure 4.10.: Measured and simulated pion efficiency as a function of momentum. This Figure has been taken from [47].

LQX-Method

The upper mentioned straight forward method is not making use of the important temporal distribution of the deposited energy. The maximal amplitude originating from the transition radiation of an electron is measured in higher time bins. With including this information to the integrated charge measurement a additional dimension is added to the particle identification approach, resulting in a bi-dimensional likelihood or L_{QX} method. The probabilities Eq.(4.5) and Eq.(4.6) are adapted to

$$P_e(E) = \prod_{n=1}^6 P^n(E_n|e) \cdot \prod_{n=1}^6 P^n(X_n|e) \quad (4.8)$$

$$(4.9)$$

leaving the likelihood definition Eq. (4.7) unchanged. With the L_{QX} method the pion suppression is improved by 15 – 30 % compared to the one dimensional L_Q method as illustrated in Fig. 4.11.

NN-Method

Although the LQX method is already a great improvement and the default pre-set way in the used AliRoot version it does not use all the information that is recorded by the detector, since only the drift time information and not the amplitude of the signal in each time bin is used. Including this additional information is however not as easy as the step from the LQ to the LQX method, since the signals in each time bin along a track are strongly correlated. The reasons herefore are the intrinsic detector signal and the response of the front-end electronics used to amplify the signals. A possibility to find an algorithm that uses all the available information is given by neural networks.

Neural networks (NN) are used for a variety of tasks, not only in particle physics, since they provide some properties that are hardly achieved in the binary world of computing. Analogous to natures example neural networks in computing consist of many simple parts so called neurons which each just performs simple operations. In the technical approach these are processors calculating weighted sums and are organised in several layers.

Since the NN method could not be used in this study, further details are referred to [48] and [49].

Comparing the pion suppression rate of the LQ, LQX and the NN method as done in Fig. 4.11 shows that the neural network approach further improves the results of the LQX method by a factor of 3-5.

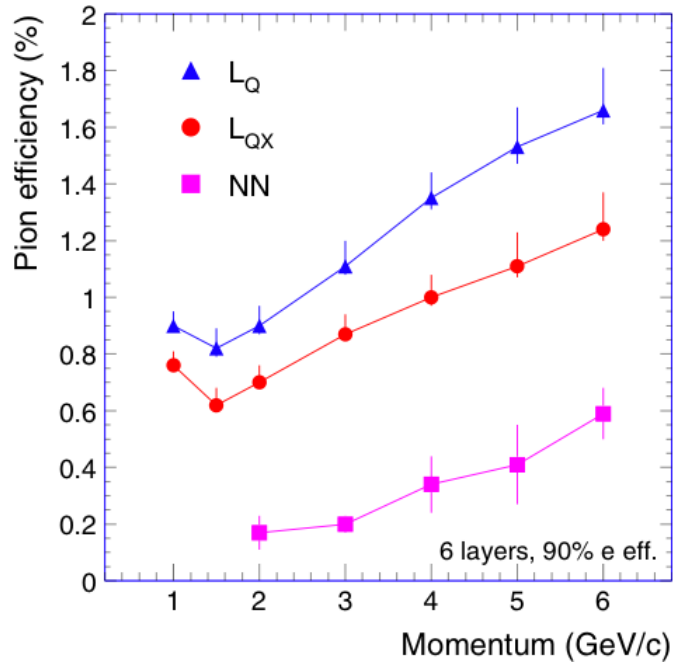


Figure 4.11.: Measured pion efficiency as a function of momentum for three different methods: likelihood based on total charge (LQ), bi-dimensional likelihood based on total charge and the position of the maximum time bin amplitude (LQX), and neural network (NN). This Figure has been taken from [47].

Combined Particle Identification

To benefit from all the particle identification information from all the sub-detectors an automatic mechanism to combine signals according to different probability densities is used.

The scheme chosen for ALICE is combining PID signals with a Bayesian approach which also allows to complete the above discussed single detector PID.

So far only the properties of a detector, the detector response functions, that do not depend on external conditions have been taken into account. The a priori probability of a particle species to even be present in the considered event is included in the improved probability $w(i|s)$ to be a particle of type i ($i = e, \mu, \pi, K, p, \dots$) if a signal s is observed in a sub-detector:

$$w(i|s) = \frac{r(s|i)C_i}{\sum_{k=e,\mu,\pi,\dots} r(s|k)C_k}, \quad (4.10)$$

where $r(s|i)$ is the detector response function and C_k the, not with $r(s|i)$ correlated, a priori probability of the considered particle type. The probabilities $w(i|s)$ are often called PID weights.

If the whole system consisting of N detectors is considered the combined PID

weights W are in the approximation of uncorrelated single detector PID measurements, given as:

$$W(i|s_1, s_2, \dots, s_N) = \frac{C_i \prod_{j=1}^N r(s_j|i)}{\sum_{k=e,\mu,\pi,\dots} C_k \prod_{j=1}^N r(s_j|k)} \quad (4.11)$$

This definition grants the advantages

- If one or several of the detectors does not identify a particle its contribution cancels out in Eq. (4.11), since all $r(s|i)$ are set equally to 0.2 for this detector.
- If several detectors get PID information, their contributions are accumulated with proper weights and therefore improve the combined PID.
- Since the a priori probabilities C_i of particles are not known during reconstruction only the probabilities determined by the single-detector response functions $r(s|i)$ are stored in the event summary data (ESD, Chap.5). The final PID decision is then postponed to the physics analysis, enabling further cuts on the quality of the particle identification.

Further, the PID depends on the chosen performed physics analysis. Nevertheless, as shown in [50] varying the true weights by 10% has only an effect of less than 3%.

The combined PID procedure in ALICE is summarised in three steps:

1. The calibration software calculates the single detector response functions $r(s|i)$.
2. The reconstruction software calculates the combined PID response, with the above features and writes the results into a file.
3. Within the analysis software the a priori probabilities C_i are estimated and the PID weights $W(i|s)$ are calculated after event and track selection.

5. ALICE Offline Framework

5.1. Overview

The ALICE Offline Framework (AliRoot) is the common framework for performance and physics studies as well as for the analysis of data for the ALICE experiment. The AliRoot framework is based on the ROOT [51] framework. ROOT is an object-oriented software package developed by CERN providing an environment for high energy physics data analysis. Aliroot makes full use of all the ROOT potential, entirely written in C++, with some external programs (hidden to the users) in FORTRAN. The framework itself, together with ROOT, is under continuous intense development. In general, there are three different steps of functionality: (1) simulation, (2) reconstruction and (3) analysis.

5.2. Monte Carlo Simulations

The AliRoot simulation framework covers the simulation of primary collisions and generation of the emerging particles, the transport of particles through the detector, the simulation of energy depositions (hits) in the detector components, their response in form of so called summable digits, the generation of digits from summable digits with the optional merging of underlying events and the creation of raw data.

Event Generation

In the absence of real data, event generators provide a realistic estimation of the abundance and kinematic distribution of particles in the final state. A virtual interface, named AliGenerator, provides access to these generators at run time since many existing event generators produce different predictions of the particle distribution at LHC energies. The virtual interface allows to study fully processed collisions, pure signal-processes events, e.g. exclusive production of hadrons consisting of c or b quarks. The program package (PYTHIA) [52] is based on a combination of analytic

results and various QCD models. Within AliRoot, it is used as an event generator for $p+p$ collision at high interaction energies. The extension to nucleus nucleus collision is realised in the program package **Heavy-Ion Jet INteraction Generator** (HIJING) [53].

Particle Transport Through the Detector

After their generation, particles in the final state are fed into the transport program after their input information is stored in a file called `kinematics.root`. Where these particles are transported through the material of each sub-detector, and the interaction with the material is simulated. At each interaction point between the particle and the material, the energy deposition and location of the interaction are stored in a data type called *hits*. This requires the simulator program to precisely know about the geometry and the material chemical composition and density of each sub-detector. A commonly used full detector simulation program is GEANT3 which is not being further developed since 1993. It is introduced into the AliRoot framework by a virtual Monte Carlo interface TVirtualMC. As alternatives, two further simulation programs GEANT4 and FLUKA are also interfaced by this virtual Monte Carlo method. For further information see [54].

Detector Response

The simulation of the detector response generates the summable digits (*sdigits*) from the energy deposition. The *sdigits* are the ideal detector response, before the digitization and threshold subtraction to digital signal format. In each sub-detector, an *sdigit* gives the signal of a channel from a given particle interaction with the material. The signal is of analog format, e.g. the voltage versus time.

Digitization

The *sdigits* are then digitised and formatted according to the output of the front-end electronics and the data acquisition system. The digitization transforms the analog signal to a digital signal and truncates it by a given threshold. The output resembles closely the real data expected to be produced by the detector. The output is in one of two forms: raw data, generated by the front-end electronics or digits containing the same information but in ROOT structures, see also Fig. 5.1. These two formats are interchangeable.

5.3. Track Reconstruction in the Central Barrel

Within the reconstruction process raw data or digits are converted into information used in physics analysis, e.g. kinematic information such as transverse momentum, pseudo rapidity and particle identification from the specific energy loss (dE/dx) in a sub-detector or time of flight. The reconstruction process in AliRoot involves three steps: clusterisation, tracking (including vertexing and particle identification) and writing the output data. The schematic flow of the reconstruction framework is shown in Fig. 5.1.

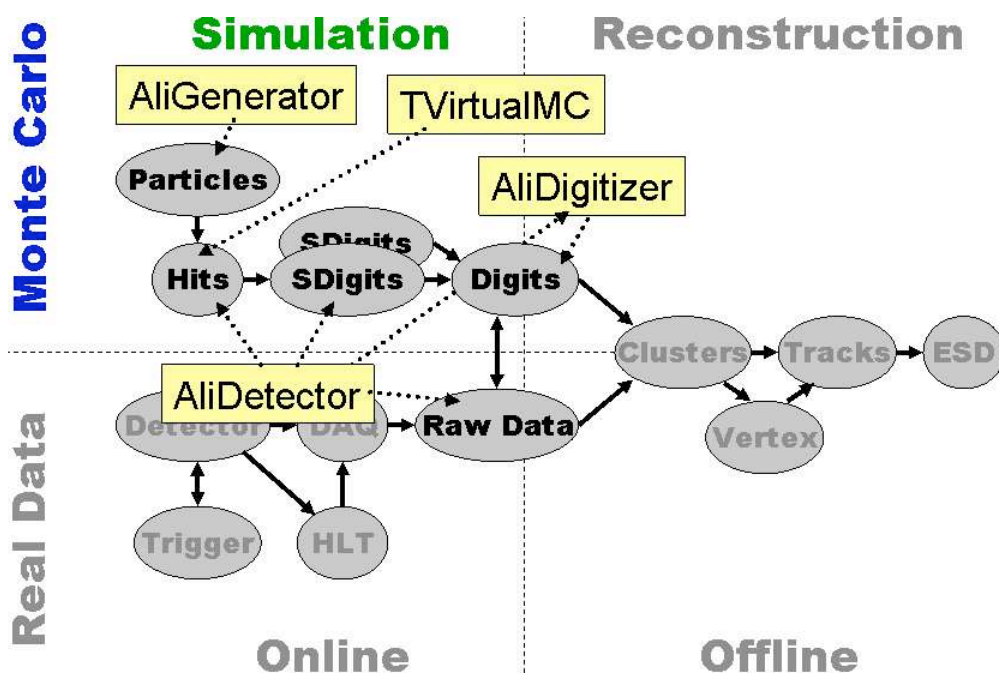


Figure 5.1.: Schematic flow diagram of Monte Carlo simulation and reconstruction in the AliRoot framework. This figure has been taken from [54].

Clusterisation

Within the first step of the reconstruction process the digits are converted into clusters by combining digits of adjacent pads that presumably originate from the same particle passing through the material. Additionally, the uncertainty of the space-point position estimation is calculated. All of the central tracker detectors (ITS, TPC, TRD) have their own detailed parameterisation of the space-point position uncertainties and cluster finding procedure. The space points together with the position uncertainties are then passed to the tracking.

If, in addition to the space point position, the detector measures the produced ionisation, this information is used for the particle identification.

Tracking

Within the tracking procedure the clusters are assigned to tracks and their kinematic properties are reconstructed including the particle's trajectory, the primary collision vertex, secondary vertices (V^0) from particle decays (e.g. $\Lambda \rightarrow p\pi$), cascade (e.g. $\Xi \rightarrow \Lambda\pi \rightarrow p\pi\pi$), kinks (like charged $K \rightarrow \mu\nu$) and particle identification information. Tracking is the main part of the reconstruction procedure and also one of the most challenging tasks of the experiment becoming even more challenging in the high multiplicity environment of a Pb+Pb collision.

Offline track reconstruction in ALICE is based on the Kalman filter approach [55]. The detector specific implementations of the track reconstruction algorithm use a set of common base classes, which make it easy to pass tracks from one sub-detector to another and test various parts of the reconstruction chain.

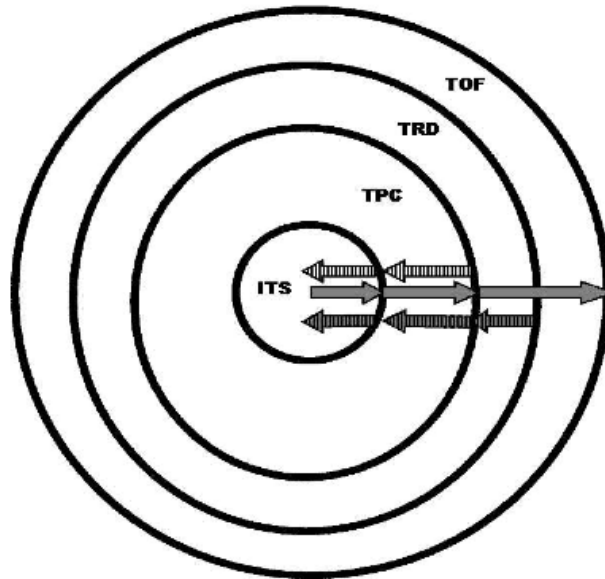


Figure 5.2.: Schematic view of the three passes of the combined track finding (see the text). This figure is taken from [56].

The single tracking steps illustrated in Fig. 5.2 are:

1. **Initial inward reconstruction pass**

The overall track finding starts with the track seeding in the outermost pad rows of the main tracking device, i.e. the TPC. Different combinations of the

pad rows are used with and without a primary vertex constraint. Typically more than one pass is performed, starting with a rough vertex constraint, imposing the primary vertex with a resolution of a few centimetres and then releasing the constraint.

Afterwards, the prolongation for each track candidate or *seed* is searched in the ITS. First, a rather strict vertex constraint with a resolution of the order of $100\ \mu\text{m}$ or better is used.

If a prolongation is found, the track is refitted releasing the constraint.

If no prolongation is found, another pass is tried, without the vertex constraint, in order to reconstruct the tracks coming from secondary vertices.

At this point it is also known which tracks are likely to be primary. This information is used in the subsequent reconstruction steps.

2. Outward reconstruction pass and matching with the outer detectors

From the innermost ITS layer the proceeding is realised with the Kalman filter described in section 5.3 in the outward direction. During this second propagation the space points with large deviation from the track fit are removed. In this way the track parameters at the outer TPC radius are obtained. The Kalman filter is continued into the TRD and towards the outer detectors: the TOF, HMPID, PHOS and EMCAL. When propagating the primary track candidates outward, their track length and time of flight are computed for several mass hypotheses. This information is used for the PID in the TOF detector.

3. Final reconstruction pass

After matching with the outer detectors, all the available PID information is assigned to the tracks. However the track momenta are estimated far away from the primary vertex. The task of the final track reconstruction pass is to refit the primary tracks back to the primary vertex or, in the case of the secondary tracks, as close to the vertex as possible. This is done again with the Kalman filter using the clusters already associated in all the detectors at the previous reconstruction passes. During this pass also the secondary vertices (V0's, cascade decays and kinks) are reconstructed. The whole tracking procedure is completed with the generation of the event summary data (ESD, see below). A typical ESD for a central Pb+Pb event contains about 10^4 reconstructed tracks, a few hundred V0 and kink candidates, and a few tens of cascade particle candidates.

Event Summary Data

After the tracking procedure is finished, all track information, consisting of the primary and secondary vertices, PID, particle kinematics and other information, is stored in the AliRoot specific Event Summary Data (ESD). The ESD is designed for

offline analysis, and is independent from the AliRoot simulation or reconstruction framework.

The reconstructed tracks are obtained from the AliESDs.root file. Each of these AliESDtracks has encoded information of how far the reconstruction was advanced. For each reconstruction step a status flag or bit is either set to true or false (0 or 1). All possibilities for the four innermost sub-detectors are summarised in table 5.1. Since TRD and ITS are not part of the inward track reconstruction, these bits are not set to true. Additionally in the used AliRoot version the flag stating that within TRD a PID is set (TRDpid) is automatically set together with TRDout since the PID information is also calculated in this reconstruction step. However, TRDpid is also set if the PID calculation does not reach a result. This feature has been discovered within this thesis and will be changed in future AliRoot versions.

name	status bit	status bit
kITSin		$2^0 = 1$
kITSout		$2^1 = 2$
kITSrefit		$2^2 = 4$
kITSpid		$2^3 = 8$
kTPCin		$2^4 = 16$
kTPCout		$2^5 = 32$
kTPCrefit		$2^6 = 64$
kITPCpid		$2^7 = 128$
kTRDin		$2^8 = 256$
kTRDout		$2^9 = 512$
kTRDrefit		$2^{10} = 1024$
kTRDpid		$2^{11} = 2048$
		(set with TRDout)
kTOFin		$2^{12} = 4096$
kTOFout		$2^{13} = 8192$
kTOFrefit		$2^{14} = 16384$
kTOFpid		$2^{15} = 32768$

Table 5.1.: Track status bits of ESD tracks stating the reconstruction progress.

Kalmanfilter

Kalman filtering [55] is a general and powerful method for statistical estimations and predictions. In the following a brief overview over the steps in Kalman filtering is given.

1. A system is determined at any moment in time t_k by a state vector x_k . The state vector varies with time according to the evolution equation

$$x_k = f_k(x_{k-1}) + \epsilon_k \quad (5.1)$$

Where f_k is a known deterministic function and ϵ_k is a random vector of intrinsic process noise which has a zero mean value ($\langle \epsilon_k \rangle = 0$).

2. **Prediction:** If, at time t_{k-1} , some estimates of the state vector \tilde{x}_{k-1} are given these estimates are extrapolated to the next time slot t_k by the formula:

$$\tilde{x}_k^{k-1} = f_k(\tilde{x}_{k-1}) + \epsilon_k \quad (5.2)$$

3. **Filtering:** If at the time t_k , together with the results of the prediction, the results of the state vector measurement are obtained, this additional information is combined with the prediction results. As a consequence, the estimation of the state vector improves with respect to the previous step.
4. The prediction and filtering steps are repeated as many times as there are measurements of the state vector.

When applied to the track-reconstruction, the Kalman-filter approach has many useful properties:

- Simultaneous track recognition and fitting.
- Rejection of incorrect space points during the one tracking pass.
- Numerical fast calculations
- Natural way to find the extrapolation of a track from one detector to another (for example from the TPC to the TRD).

6. J/ψ Analysis

In the previous chapters the importance of the J/ψ meson as a probe for the quark-gluon plasma, the capabilities of the ALICE detector, especially the TRD and the AliRoot framework that allows the analysis of simulated and real data were introduced.

In this chapter the detection of J/ψ mesons via the decay channel $J/\psi \rightarrow e^+ + e^-$ in the ALICE detector is investigated. For this purpose two completely independent data sets are used to ease the understanding of the reconstruction and analysis selection steps and the large computing time needed for the background analysis. One data set is a pure J/ψ signal whose basic features are described in section 6.1. The other data set is used for combinatorial background estimates and consists of minimum bias events simulated for $p+p$ collisions with a centre of mass energy of $\sqrt{s} = 10$ TeV generated with PYTHIA. More details are presented in section 6.6. The first step in the reconstruction of a J/ψ meson is the selection of single track candidates. This involves selections on the track quality and PID quality and its topology. This is discussed in more detail in section 6.2 and are also considered when obtaining the background. The obtained J/ψ invariant mass distribution with these selections is presented in section 6.3 followed by the discussion of the detector's reconstruction efficiency and resolution.

6.1. J/ψ Monte Carlo Input

In this section the settings and the resulting Monte-Carlo input of the simulation containing the J/ψ signal are summarised.

The p_T parameterisations presets for J/ψ mesons that are available in AliRoot are illustrated in Fig. 6.1. The differences of the p_T spectra are the lower limits at which the p_T distribution starts, the position and height of the maximum and the slope. The functions are taken directly from the source code of the `AliGenMuonlib` [54] class but scaled as summarised in Table 6.1. The additional setting for a flat J/ψ p_T distribution is not considered here.

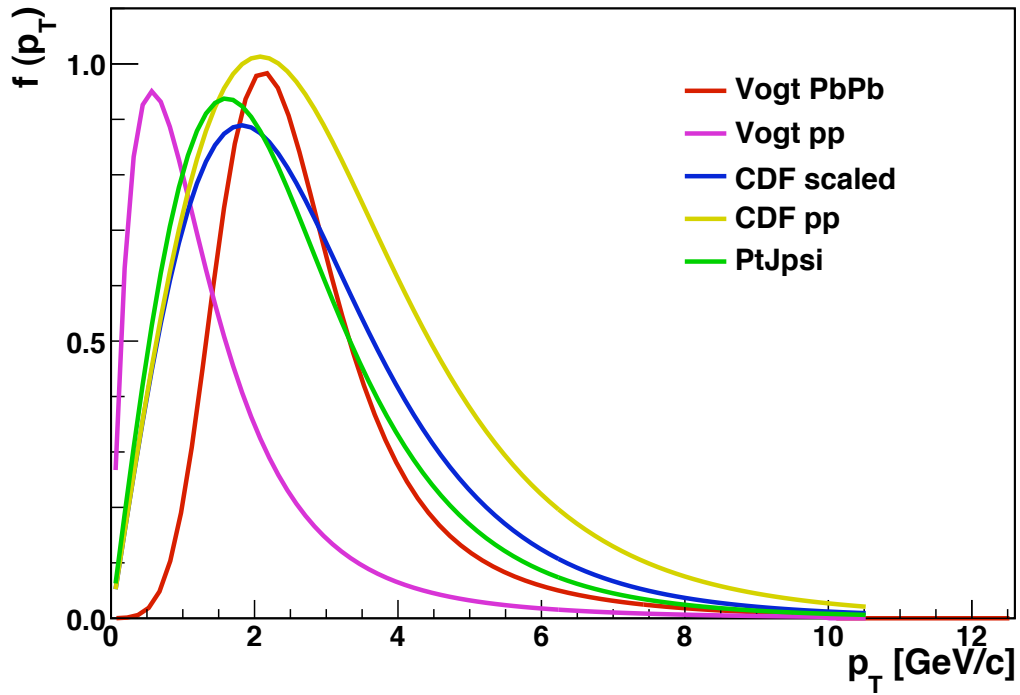


Figure 6.1.: Scaled p_T parameterisations available in AliRoot for J/ψ . The scale factors are listed in Tab. 6.1.

variable	p_T parameterisation	1/scale factor
Vogt or Vogt PbPb	PtJpsiPbPb	140
Vogt pp	PtJpsiPP	1000
CDF scaled	PtJpsiCDFscaled	1.2
CDF pp	PtJpsiCDFscaledPP	1.2
else	PtJpsi	1

Table 6.1.: p_T parameterisations available in AliGenMuonLib for J/ψ and the factors used to scale these functions in Fig. 6.1.

The initial p_T distribution used in the simulation of the J/ψ signal is left to the default settings found in the AliRoot example configuration 'pptest' being "Vogt PbPb". Further the following settings are applied:

- per event solely one J/ψ is generated at the primary vertex without any further particles. This simplifies the understanding of the data, the detector response and the influence of every track selection step. Furthermore in principle no Monte-Carlo (MC) tagging is needed to reconstruct J/ψ mesons without huge combinatorial background.
- each J/ψ is forced to decay into an e^+e^- pair since this is the decay channel of interest within this work.
- the rapidity range of the generated J/ψ mesons is $|y| \leq 1$, since the focus of this analysis is at the detectors of the central barrel, especially the TRD, an acceptance of $|y| < 0.9$ is not exceeded.

The MC generated J/ψ p_T distribution originating from the "Vogt PbPb" parameterisation of about 100k events is shown in Fig. 6.2. The p_T distribution starts to rise significantly above $p_T > 0.5$ GeV/c reaches its maximum around 2.5 GeV/c and decreases strongly at larger p_T . This leads to limited statistics for low and high momenta for the efficiency study.

The rapidity distribution is flat with a cut-off at $|y| = 0.9$ as shown in Fig. 6.3. The transformation from rapidity and transverse momentum into pseudo-rapidity (Fig. 6.4) leads to a dip at $\eta \approx 0$ as well as a rapid drop of the distribution for $|\eta| > 1$.

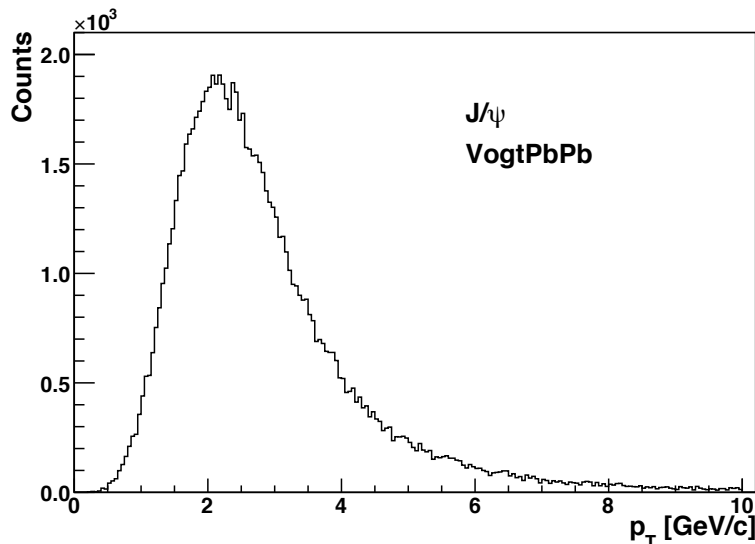


Figure 6.2.: MC transverse momentum distribution of about 100k simulated J/ψ mesons with the p_T parameterisation "Vogt Pb Pb".

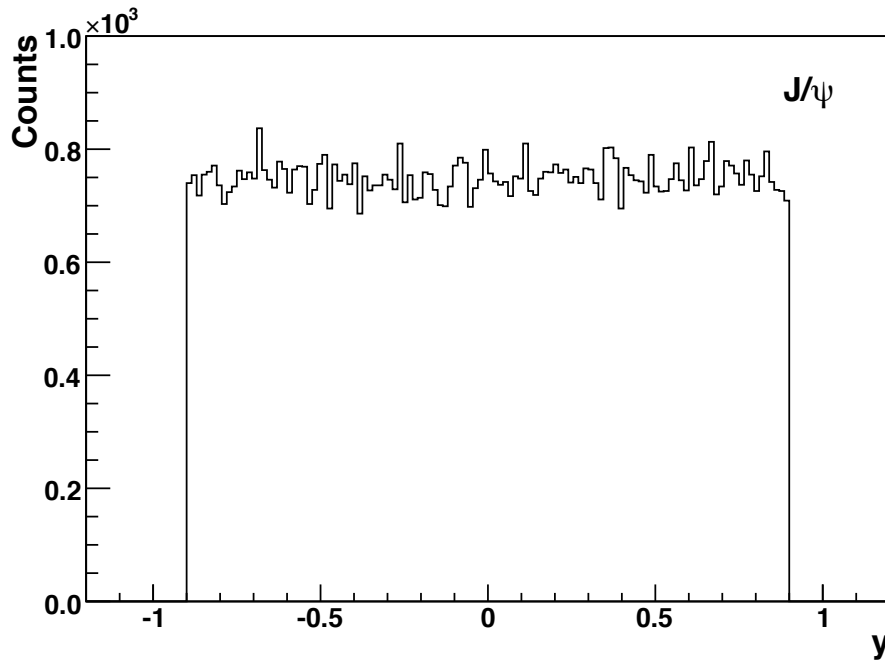


Figure 6.3.: MC rapidity distribution y of about 100k simulated J/ψ mesons with the preset $|y| < 0.9$.

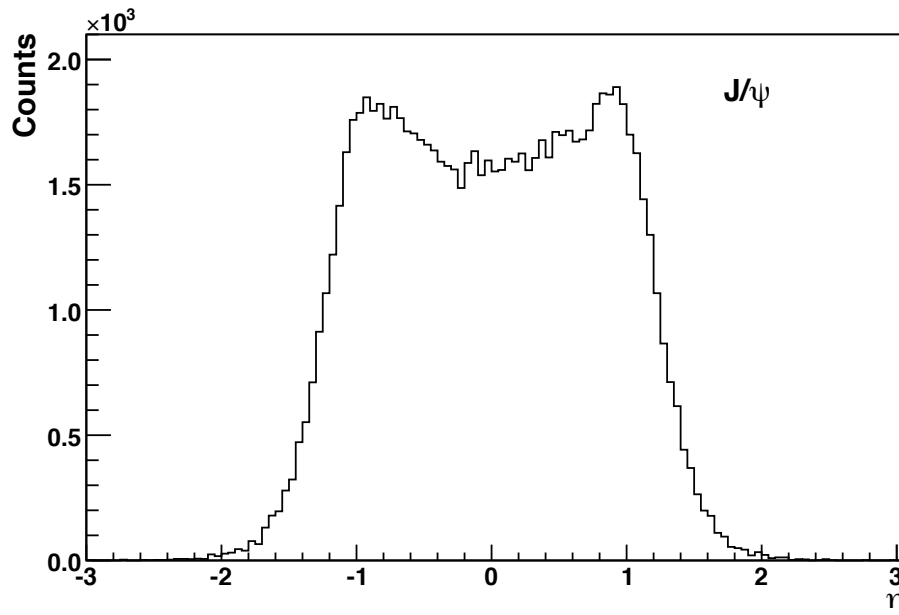


Figure 6.4.: MC pseudo-rapidity η distribution of about 100k simulated J/ψ mesons.

The MC p_T distributions of the electrons (blue) and positrons (red) are shown in Fig. 6.5 for e^\pm within the rapidity range $|y| < 0.9$. The electrons and positrons are selected to originate directly from the generated J/ψ to ensure that they originate from the primary vertex. The maximum of this distribution is found at less than 1 GeV/c followed by a bump at $p_T \approx 2$ GeV/c. The distribution resembles the overlap of two single distribution one with its maximum at 2 GeV/c and another narrower one with a peak at 1 GeV/c possibly due to edge effects from the initial J/ψ distribution in rapidity.

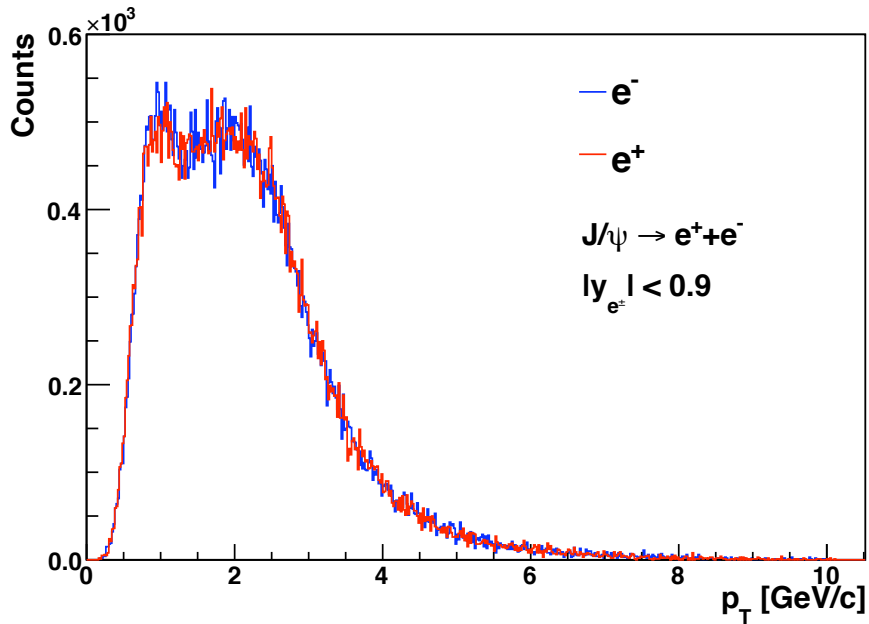


Figure 6.5.: MC p_T distribution of e^+e^- from J/ψ in the rapidity range $|y| < 0.9$.

The x - and y -coordinates of the production vertex of every electron for about 10k J/ψ signal events obtained from MC are shown in Fig. 6.6. The large number of secondary electrons e.g. from Bremsstrahlungs photon conversions reveals the structure of the implemented detectors e.g. the 6 TRD layers, and material budget. Not only the detectors from the central barrel but also support structures are visible.

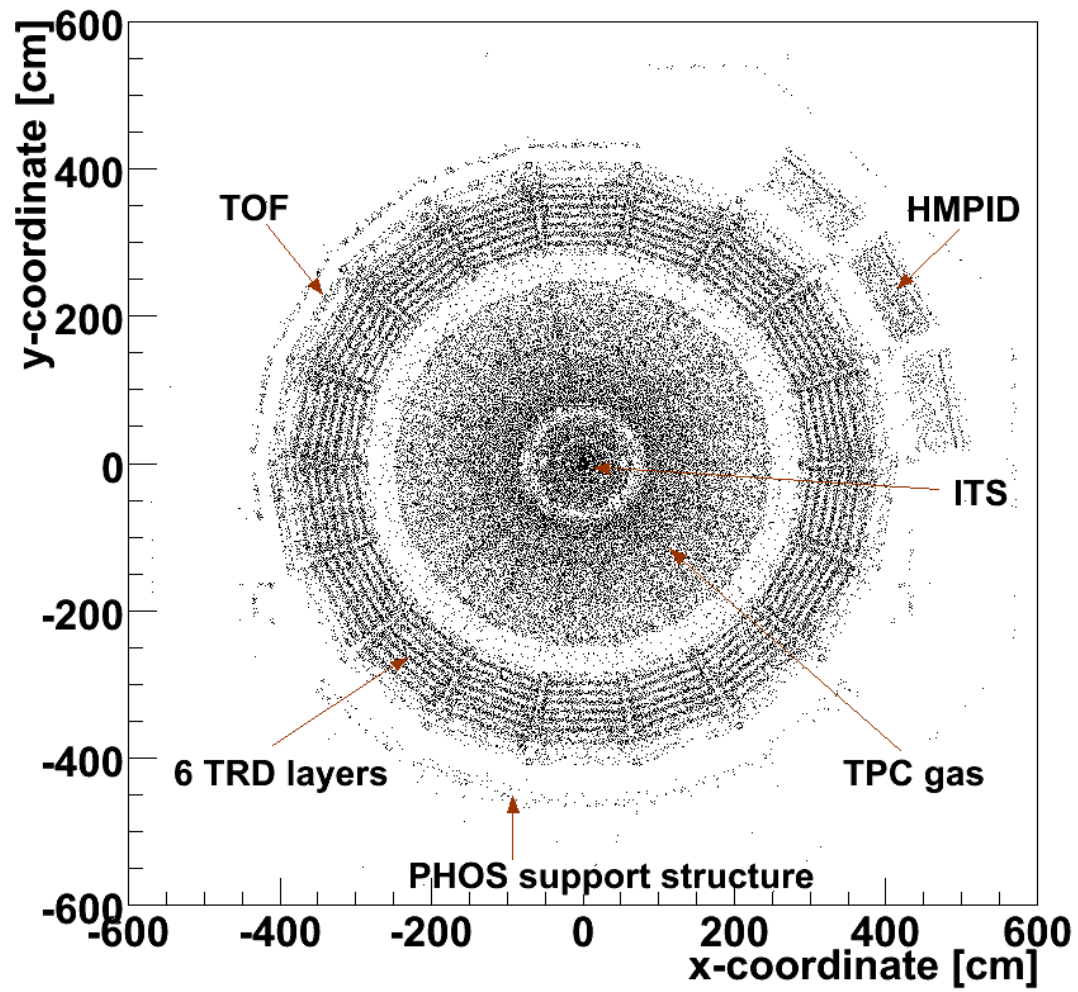


Figure 6.6.: The MC production vertex of all primary and secondary electrons and positrons in about 10k J/ψ events.

6.2. Single Track Selection

In every Event Summary Data (ESD) the information of 100 events is stored. Nevertheless the AliAnalysisTask framework ensures the event by event access and analysis. From the reconstructed tracks (AliESDtrack), stored within the ESDs, all the information like transverse momentum p_T , pseudo-rapidity η and particle identification information that real, non-simulated data has, is extracted. Furthermore a label is obtained to relate every ESDtrack to the MC particle it corresponds to.

To select track candidates for the reconstruction of a J/ψ several criteria are applied. First of all only tracks from the J/ψ , produced at the origin of the global ALICE coordinate system, i.e. from the interaction point, are taken via the MC truth information. Secondly only tracks within the rapidity range $|y| < 0.9$ are selected. To later on compare the MC input data with the reconstructed one, this information is also taken from the corresponding MC particle. All other selected properties are obtained from the reconstructed data, not the MC information. The selection criteria of single tracks are:

1. kink topology
2. reconstruction status
3. PID quality

Kink Topology

A secondary vertex at which only one charged daughter track is detected while the other charge neutral daughter is not detected in gas detectors, is called a *kink*. Within reconstruction of the track, a kink often manifests itself as a continuous track with a sudden turn or “kink”. The deflection angle depends on the relative momentum of the undetected daughter and the momentum of the mother particle. For instance particles with rather long lifetimes may decay in the TPC, e.g. $K^+ \rightarrow \mu^+ + \nu_\mu$. As a result, the track of the charged K^+ and the daughter μ^+ is reconstructed as a single track with a kink structure. The kink topology occurring in this work is the radiation of Bremsstrahlung: $e^- \rightarrow e^- + \gamma$.

An algorithm in AliRoot identifies the daughters with momentum up to 3 GeV/c in the TPC. At higher momenta, the deflection angle is generally too small to be detected by the track fitting algorithm. The specifics of the implementation, thresholds and output of this algorithm are not fully understood and currently under investigation. Nevertheless, daughters from kink topologies marked by the kink algorithm of the used AliRoot version (v4-13-Rev-01) are rejected in this analysis to reduce the amount of secondary and wrongly assigned tracks.

Track Quality

As described in Chap. 5 each reconstruction step is represented by a single status bit. Each status bit is set to true (1) or false (0) indicating the progress of the tracking and PID steps. Figure 6.7 shows the distribution of the status bits that were set to true for ESDtracks from the primary vertex and within the rapidity range $|y| < 0.9$ of about 100.000 events. The four most left bars show the entries of the status bits ITS_{in} , ITS_{out} , ITS_{refit} and ITS_{pid} (from left to right) followed by the entries of the same status for TPC, TRD and TOF. As explained in Chap. 5 the reconstruction starts with fitting inwards from the outer regions of the TPC. Therefore the TPC_{in} bit is set first and reflects the upper limit of an overall reconstruction efficiency. All four possible status bits are almost equally set for TPC and ITS. Since there is no inward fitting for the other sub-detectors the “in” bit is never set to true for TRD and TOF. Additionally TRD_{out} and TRD_{pid} are set simultaneously in the used AliRoot version. Hence, the TRD_{pid} bit does not ensure that the PID information in the TRD is sufficient to distinguish between different particle species. Since TOF was not used explicitly its settings are not discussed any further.

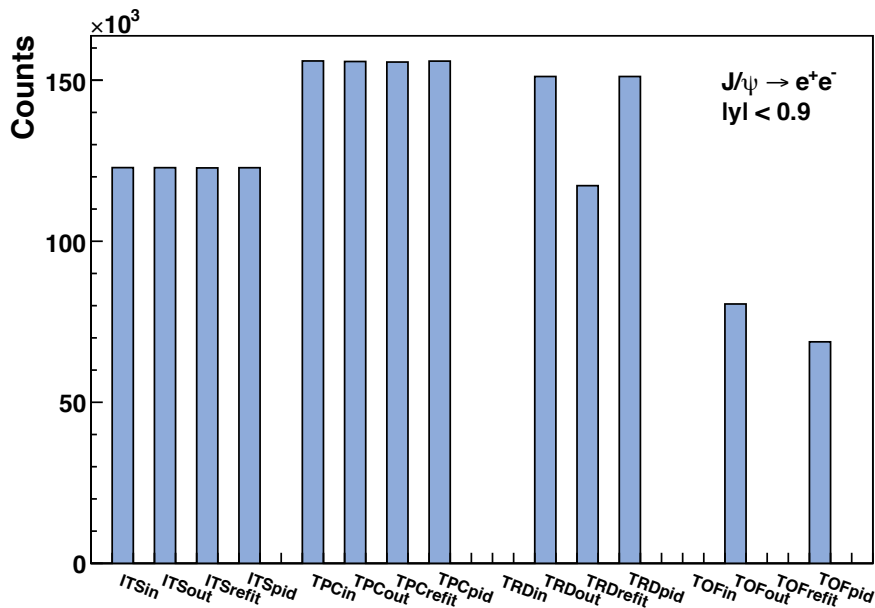


Figure 6.7.: Status bits of electron ESDtracks from the primary vertex and rapidity $|y| < 0.9$ of about 100k J/ψ events.

In general, the more space points are assigned along a particle trajectory, the better is the quality of the fitted track. Also, measurements at a different radius, i.e. with different sub-detectors, improve the accuracy of the tracking. The cuts on

the quality of the track are only implicitly related to the underlying physics of the process, but ensure that the information used for the analysis is reliable and the reconstruction of the event worked properly. For this purpose the `TPCrefit` status bit is required. To get a better insight into the TRD geometrical acceptance and the selection step described next, the `TPCrefit` is also required.

TRD PID Quality

Since the $J/\psi \rightarrow e^+ + e^-$ reconstruction depends crucially on the ability of the TRD to identify single electrons a variable stating the quality of the obtained PID signal is of need. The discussed track status cuts almost exclusively aim at the tracking not the particle identification. As described in Chap. 4 the pion efficiency of the TRD depends, with a factor two per layer, strongly on the number of layers in which a measured signal assigned to a track is used for PID calculations. Therefore a variable called `TRDpidQuality` stating this number is available for every `ESDtrack`. The distribution of this variable is plotted in Fig. 6.8.

In 18.7% of the cases the `TRDpid` status bit is set even for tracks without any assigned cluster in one of the TRD layers. To ensure good electron efficiency the number of layers is further on required to be maximal (`GetTRDpidQuality() == 6`). For the analysed data sample about 73.3% of the tracks with `TRDrefit` meet this requirement. To ensure a maximal pion suppression the `TRDpidQuality` is required to be maximal `TRDpidQuality = 6` in the following.

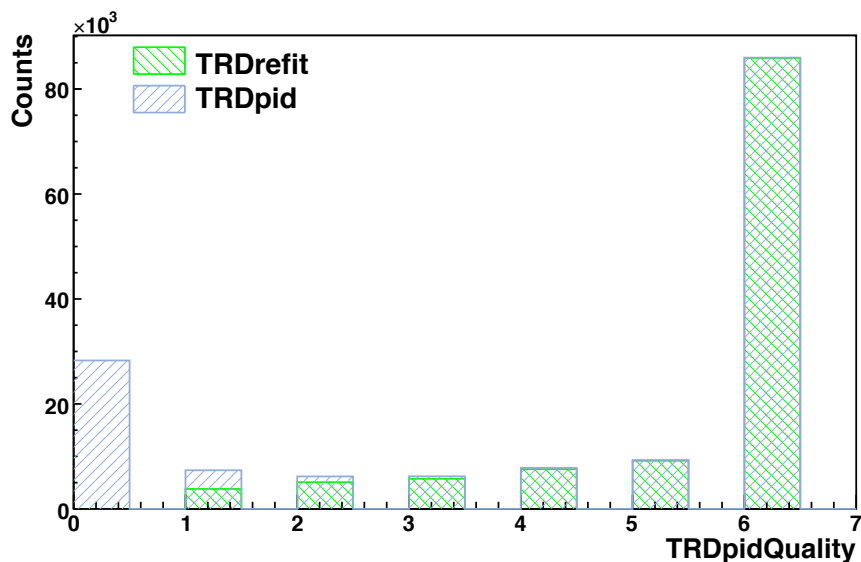


Figure 6.8.: Number of layers with hits used for PID in the TRD of e^\pm from the primary vertex with rapidity $|y| < 0.9$ for tracks with `TRDrefit` (green) and `TRDpid` (blue).

Cut Influences

The p_T distribution of electrons after reconstruction is shown for the above discussed cuts in Fig. 6.9. Making use of the MC information only tracks from the primary vertex and within the rapidity range $|y| < 0.9$ are selected. With the kinks sorted out (cyan) the p_T distribution resembles strongly the one of the MC input Fig. 6.5. Selecting tracks with `TPCrefit` set, additionally (magenta) only a small amount of tracks are sorted out. Further the strong influence of the `TRDrefit` cut (green) is observed. Not only does the distribution start at the geometric acceptance threshold of $0.3 \text{ GeV}/c$ but the shape changes slightly since the peak at $p_T \approx 1 \text{ GeV}/c$ becomes less pronounced. This trend increases if only tracks with additionally 6 layers used for PID in the TRD are selected (blue). All these cuts reduce the spectrum height from initially about 500 counts at the p_T region $1 \text{ GeV}/c < p_T < 3 \text{ GeV}/c$ to less than 300 counts.

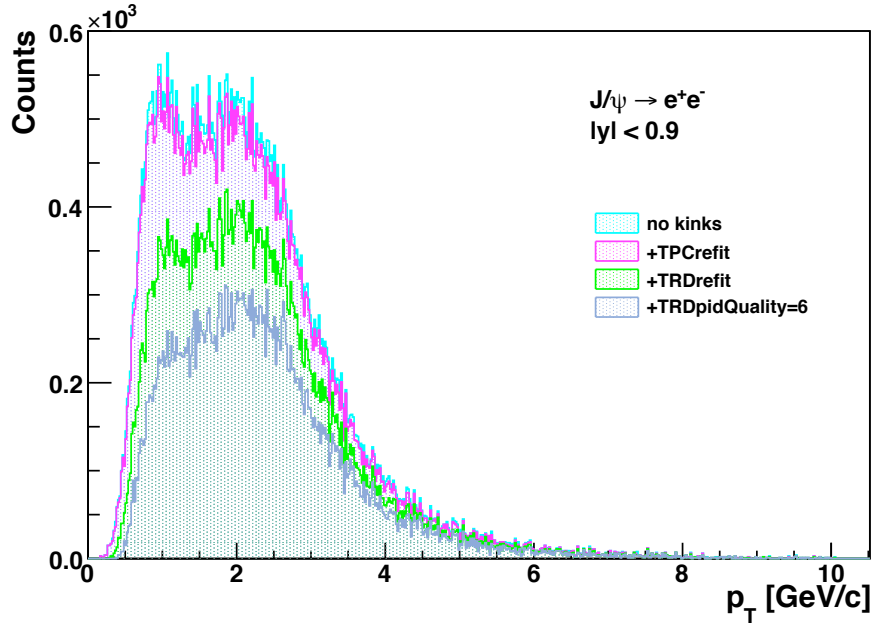


Figure 6.9.: Reconstructed p_T distribution for electrons directly from J/ψ with $|y| < 0.9$ for different cuts as discussed in the text.

Figure 6.10 shows the pseudo-rapidity distribution of electrons from the primary vertex for the same cuts. Requiring the `TPCrefit` status flag set (magenta) reduces the amount of entries only little in the region $|\eta| < 1$ in respect to the case with only the kinks sorted out. The `TRDrefit` cut (green) displays its strong influence due to the geometric acceptance of the TRD. On the one hand the minimum rapidity of $|y| < 0.9$ to reach the TRD manifests as a clear cut off.

On the other hand the four gaps between the stacks of the TRD along z -direction

(see Chap. 4) become visible as well as a decrease of the number of reconstructed tracks in a small region around $|\eta| = 0$. This decrease is due to missing TRD stacks at $\eta = 0$ for super-modules in sectors 13,14,15. These are left out to minimise the material budget seen by the PHOS spectrometer which is located at larger radial position behind the TRD in the ALICE experiment. This decrease is further on referred to as the “PHOS hole”. For tracks with $\text{TRDpidQuality}=6$ (blue) these effects are even more pronounced.

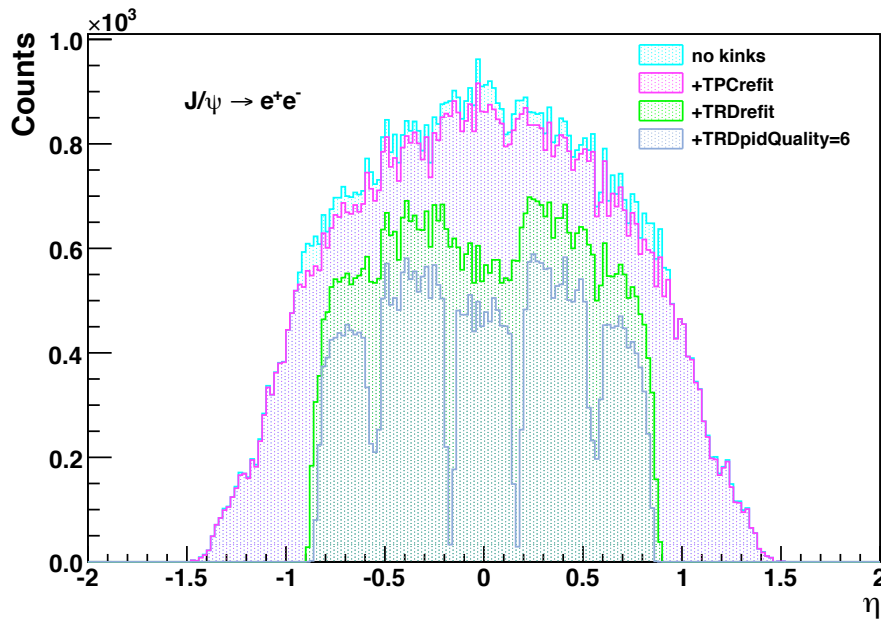


Figure 6.10.: Reconstructed pseudo-rapidity distribution for electrons directly originating from the decay $J/\psi \rightarrow e^+e^-$ for cuts discussed in the text.

The distribution as a function of pseudo-rapidity η and transverse momentum p_T of reconstructed electron tracks is shown in Fig. 6.5. The distribution in η falls quickly from low p_T on due to the initial rapidity distribution. The small dip at $\eta \approx 0$, $p_T \approx 0$ GeV/ c is due to the geometric acceptance. The peak at $p_T \approx 2$ GeV/ c and $\eta \approx 0$ stands out while the contribution to the above (Fig. 6.9) observed peak at $p_T \approx 1$ GeV/ c is spread over a larger η region.

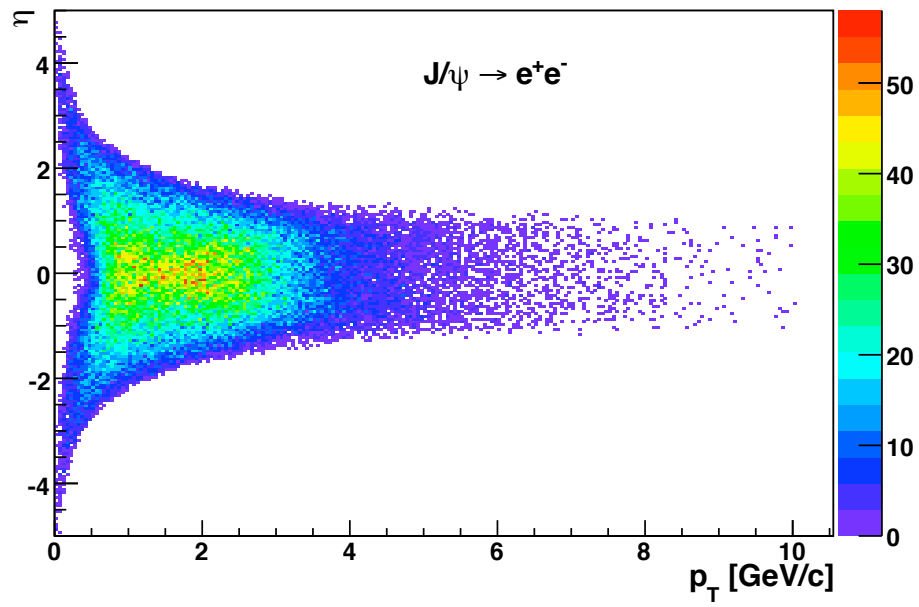


Figure 6.11.: Reconstructed pseudo-rapidity η distribution versus transverse momentum p_T for electrons from the primary vertex.

6.3. Invariant Mass Calculation

Generally, to reconstruct a J/ψ meson, the invariant mass of all decay particles is calculated. Therefore not only the e^+e^- pair from the primary vertex but also all further decay products from secondary vertices are added.

For real data, information that allows a complete invariant mass reconstruction is not available. Therefore every reconstructed track is combined with each track of opposite charge if both fit the required properties discussed below. This already leads to purely combinatoric background.

However, to study a clear J/ψ signal and to avoid the, due to the configuration of the signal simulation small, combinatoric background the available Monte-Carlo (MC) information is taken to select only tracks from the same decay, the same mother particle. Background estimates are considered separately in section 6.6.

Further the Kalman-Filter (KF) package [57] in Aliroot is used. Every track from the ESD is taken together with a particle identity prognosis to recalculate the particle's path through the detector and to create a member of this package, a `AliKFParticle`. The main purposes of this package is to achieve a better vertex resolution since different particle assumptions lead to energy loss and helix parameter corrections. Additionally error estimates of the track parameters are provided by the KF package. The already implemented possibility to combine two `KFParticle`s into one by calling the correct constructor is taken for the invariant mass calculation. The Kalman filter is described in Sec. 5.3.

The prerequisites for a track to be taken for the invariant mass calculation are, additionally to the decay mother, the rapidity $|y| < 0.9$, taken from the `ESDtrack` and the PID information for the `KFParticle` creation, taken from the MC input.

Despite all efforts, persistent inconsistencies in the implementation of the TRD PID algorithm in AliRoot simulation, the PID was not available for this work.

The Likelihood distribution obtained in TRD for electrons with $1 \text{ GeV}/c < p_T < 2 \text{ GeV}/c$ is shown in Fig.6.13. The rise for low probabilities and the pronounced peak at $L = 0$ are due to inaccurate implementation in the AliRoot TRD PID framework and are corrected in newer AliRoot versions. Nevertheless choosing a p_T dependent cut off value in the analysis to ensure 90% electron efficiency is prevented. Figure 6.13 shows the likelihood values after which 90% of the electrons are found. In the example of Fig. 4.8 from [45] the L -value corresponding to 90% electron efficiency is $L \approx 0.89$.

The reconstructed J/ψ invariant mass distribution is shown in Fig. 6.14. Clearly the peak at the J/ψ mass $m \approx 3.1 \text{ GeV}/c^2$ stands out. The full width of the peak at half maximum is $\text{FWHM} \approx 60 \text{ MeV}/c^2$ in the case of all applied cuts (blue). Further resolution details are discussed in Sec. 6.5.

Also well visible is the asymmetry of this peak. This *Bremsstrahlung tail* emerges due to electrons and positrons from the J/ψ decay, emitting Bremsstrahlung as described in Chap. 4. Due to emitted radiation, the energy lost by the electron

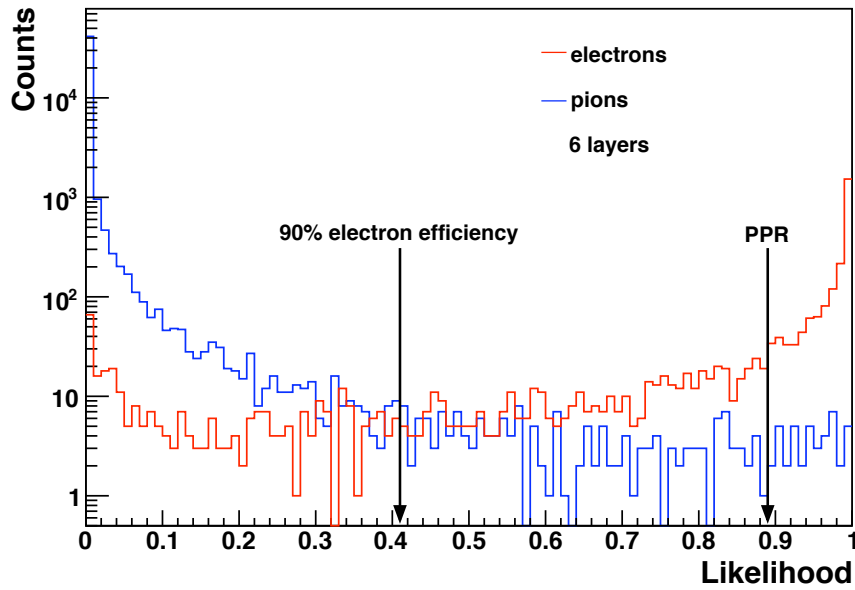


Figure 6.12.: TRD likelihood distribution for electrons (red) and pions (blue). The right arrow indicates the exemplary value shown in Fig. 4.8 and the left arrow the value obtained in this sample. Several p_T bins are combined for this Figure for statistics reasons.

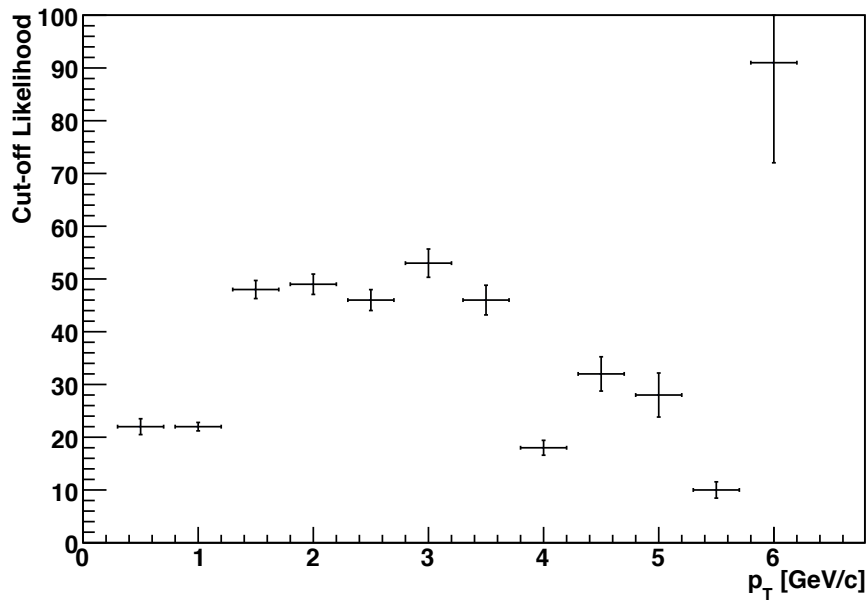


Figure 6.13.: Likelihood values in percentage for 90% electron PID efficiency versus transverse electron momentum.

is missing when calculating the invariant mass. This results in the observed lower invariant mass. Since the the Bremsstrahlungs photon can carry any fraction of the electron, the radiation tail is continuous. To roughly estimate the amount of reconstructed J/ψ mesons in the tail a simplified definition of the tail is taken to be the area from $0.5 \text{ GeV}/c^2$ up to 2.8 or $3.0 \text{ GeV}/c^2$. The ratios of the J/ψ mesons in the tail in respect to the total yield of reconstructed J/ψ being the integrated area above $0.5 \text{ GeV}/c^2$ with the different applied cuts are listed in Table 6.2 and Table 6.3. The definition of the tail is of tremendous influence. However, the ratio of J/ψ mesons in the radiation tail becomes smaller the more restrictive the cuts get.

The observed ratio of J/ψ mesons in the tail is by a few percent systematically

cuts	J/ψ in tail
no kinks	49.9%
TPCrefit	49.1%
TRDrefit	44.0%
Trdpidquality= 6	41.6%

Table 6.2.: Ratio of J/ψ mesons in the tail from 0.5 to $3.0 \text{ GeV}/c^2$.

cuts	J/ψ in tail
no kinks	32.9%
TPCrefit	32.4%
TRDrefit	25.9%
Trdpidquality= 6	23.2%

Table 6.3.: Ratio of J/ψ mesons in the tail from 0.5 to $2.8 \text{ GeV}/c^2$.

higher than the 20 % other recent studies for the ALICE experiment imply. The difference is explained by an incorrect implementation of the ITS geometry, which is overlapping, in the used AliRoot version `v4-13-Rev-01`, resulting in a higher radiation length. Therefore the probability of particles to interact with the traversed material as described in Sec. 4.1. For this reason their mean energy loss is increased. This bug is fixed in recent AliRoot versions and will be considered in future studies. Within the background of $p+p$ collisions the tail is not recognised, since the additional counts from the J/ψ tail are much lower than the background. Therefore larger statistic uncertainties arise because of the Bremsstrahlungs tail as sketched in section. 6.6. The loss of J/ψ mesons in the tail is estimated while the J/ψ invariant mass peak is fitted with a Gaussian function.

Bremsstrahlungs photons from electrons convert in the detector material to electron-positron pairs $\gamma \rightarrow e^+ + e^-$. Reconstructing the invariant mass of these pairs and therefore the zero rest mass of the photon leads to the peak around zero in the invariant mass plot.

The bump from about $0.05 \text{ GeV}/c^2$ up to $0.5 \text{ GeV}/c^2$ is due to two decay correlations originating from combining the initial electron (positron) with the positron (electron) in the final state of the process $e^\pm \rightarrow e^\pm + \gamma \rightarrow e^\pm + e^+ + e^-$ and therefore combining an electron from the J/ψ with one low momentum electron from a Bremsstrahlungs photon. Since the MC information was used to select particles to come from the same mother, this distribution also displays that more than one ESDtrack is related to one MC particle.

Further the cuts discussed in the previous sections are applied to every track taken for the invariant mass calculation. Since now the probability of two tracks to meet the required properties enter, the cut effects on the resulting spectra are more pronounced.

The difference between the selection of tracks with `TPCcrefit` (magenta) and only the kinks sorted out (cyan) is minimal. The influence of the `TRDrefit` cut (green) is more distinct and excludes already almost all reconstructed Bremsstrahlungs photon and two decay correlations while after the `TRDpidQuality` cut (blue) only the J/ψ peak is left. The peak is reduced from about $5 \cdot 10^3$ counts for the first two cuts to about $3 \cdot 10^3$ counts for the `TRDrefit` and to about $1.5 \cdot 10^3$ counts with all cuts applied.

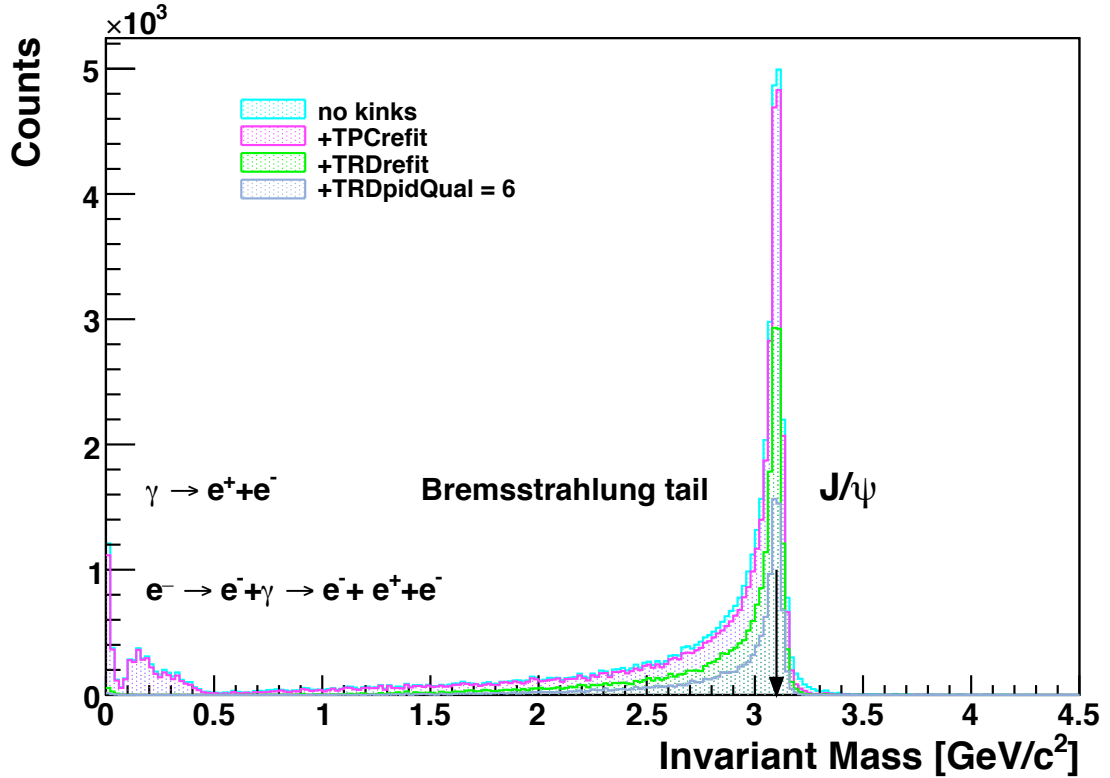


Figure 6.14.: Reconstructed invariant J/ψ mass spectrum for the track cuts discussed in the previous section.

6.4. Efficiency Studies

The efficiency ϵ is defined as the number of reconstructed particles divided by the number of generated particles.

$$\epsilon = N_{J/\psi \rightarrow e^+e^-}^{rec}(p_{T,i}) / N_{J/\psi \rightarrow e^+e^-}^{sim}(p_{T,i}) \quad (6.1)$$

$$= N_{J/\psi \rightarrow e^+e^-}^{ESD}(p_{T,i}) / N_{J/\psi \rightarrow e^+e^-}^{MC}(p_{T,i}) \quad (6.2)$$

The efficiency errors are calculated binomially because the errors of the used bins are correlated, since the existence of a MC entry is the precondition to find a reconstructed entry. With e_1, e_2 being the bin errors of histogram 1, 2; b_1, b_2 being the bin content of histogram 1, 2 and $w = b_1/b_2$ the error $\Delta\epsilon$ is calculated basically as:

$$\Delta\epsilon = |w(1-w)/b_2| \quad (6.3)$$

or improved to work with weighted histograms and implemented in ROOT:

$$\Delta\epsilon = |((1-2w)e_1^2 + w^2e_2^2)/b_2^2| \quad (6.4)$$

Working without weights and asymmetric errors the binomial error is zero if both, MC and reconstructed bins have the same amount of entries, $b_1 = b_2$.

To avoid the over- or underestimation of p_T or η bins due to the reconstructed values not being the same as in the original MC data, the corresponding MC values are taken for reconstructed tracks meeting the requirements discussed in the previous sections.

Figure 6.15 shows the efficiency of single electron tracks from about 100k J/ψ mesons in the momentum range $0 \text{ GeV}/c < p_T < 6 \text{ GeV}/c$. Both MC as well as reconstructed tracks are selected to be from the primary vertex and within the rapidity range $|y| < 0.9$. These constraints eliminate the lowest p_T contribution as seen in Fig. 6.5 and Fig. 6.9. Therefore the starting point of the distribution is at $p_T \approx 0.3 \text{ GeV}/c$.

With only the kinks sorted out (cyan) an almost over the whole range constant efficiency of 105% is found. This constant overestimation has several origins. At lowest p_T , tracks curve in the magnetic field thus reentering one of the sub-detectors. At $p_T > 3 \text{ GeV}/c$ kinks are no longer identified and therefore kink daughter and mother are related to the same MC track. Generally relating the ESDtracks to their MC pendants often creates multiple artificial entries in the same bin since daughter tracks, as from Bremsstrahlung, are still related to the same MC p_T bin of their mother. Details are still under investigation.

Almost all primary tracks with rapidity $|y| < 0.9$ are well reconstructed in the TPC (magenta).

The efficiency curve of reconstructed tracks with the status TRDrefit (green) quickly

risers due to the geometric acceptance, from $p_T = 0.3$ GeV/ c on and saturates at about 80%. The even stricter cut of having six layers used for the PID calculation leads to a slower rise and a saturation of only little lower values. For low and higher p_T bins the statistics is smaller resulting in higher error bars. More precise saturation values integrated over the range $1 < p_T < 6$ [GeV/ c] are summarised in Table 6.4.

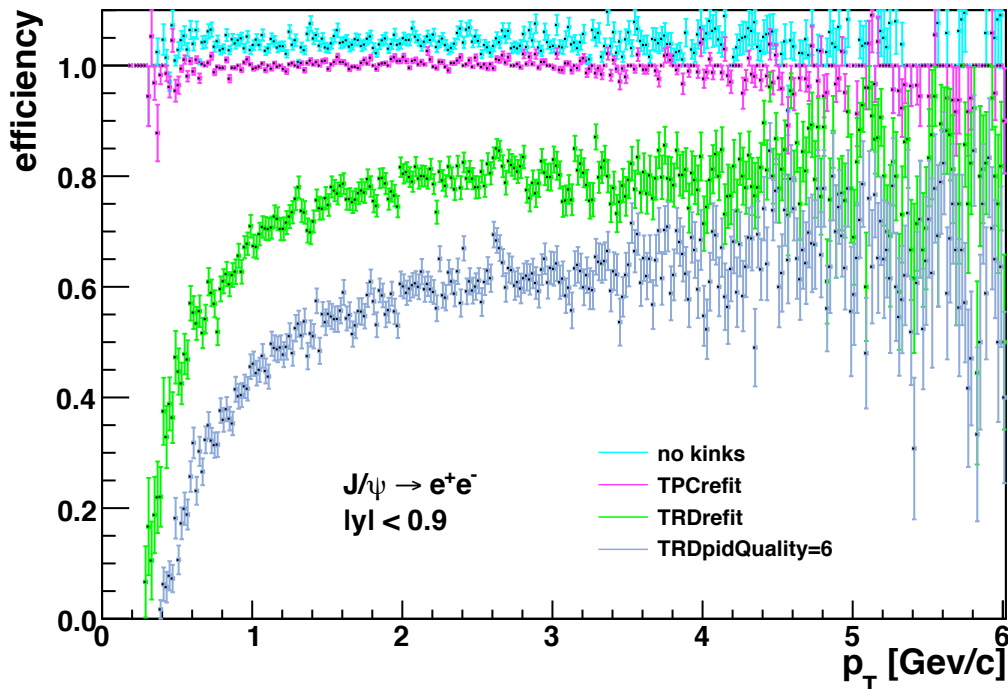


Figure 6.15.: Reconstruction efficiency of single electron tracks in the p_T region $0 < p_T < 6$.

The efficiencies as a function of pseudo-rapidity η is shown in Fig. 6.16 and is obtained analogous to the efficiencies as a function of p_T but without the track prerequisite $|y| < 0.9$. The efficiencies in pseudo-rapidity show saturation after a quick rise at almost the same values as in the p_T case.

In the case with only kinks sorted out (cyan) the same overestimation is observed as well as the almost 100% reconstruction efficiency of tracks within the TPC (magenta). The small peak at $\eta = 0$ originates from numerical errors in the calculation of η . A geometric acceptance effect of the TPC central electrode, section. 3.2, is not observed. In the case of TRDrefit (green) required the TRD geometric acceptance becomes clearly visible, showing the acceptance in pseudo-rapidity of $|\eta| < 0.9$ as well as the PHOS hole reducing the number of reconstructed tracks by almost 20% in the region $\eta \approx 0$ and the gaps between the TRD stacks. Especially the effect of

these gaps is even more pronounced after the TRDpidQuality= 6 cut. Within the acceptance of the detector the distributions are constant at $\epsilon \approx 0.8$ and $\epsilon \approx 0.65$. Mean integrated numbers of the range $|\eta| < 0.8$ are shown in Table 6.4.

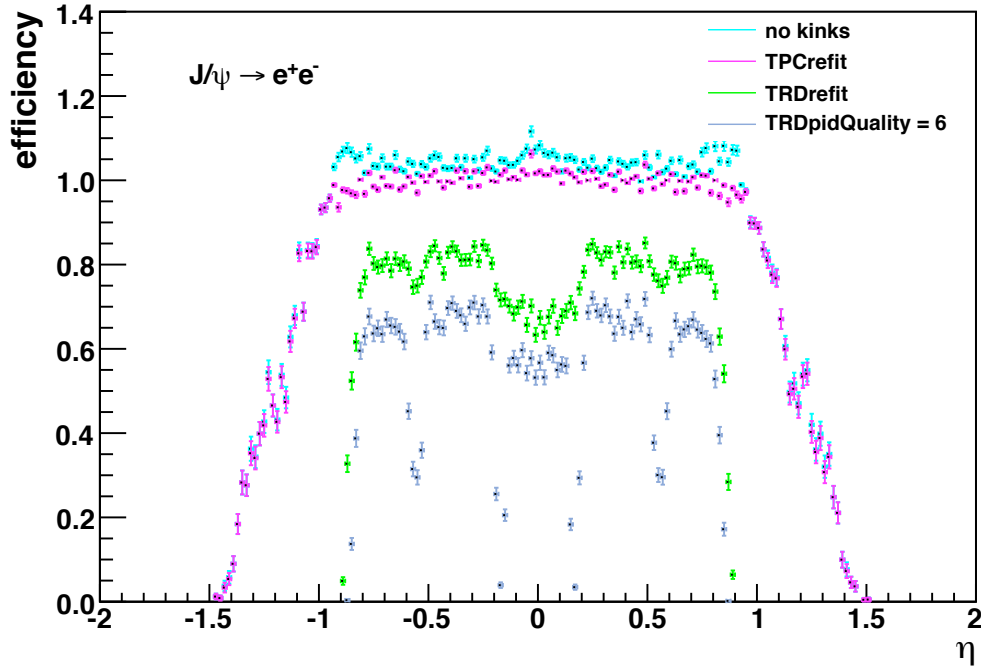


Figure 6.16.: Reconstruction efficiency of single electron tracks in the pseudo-rapidity region $|\eta| < 2$.

cuts	p_T	η
	efficiency [%]	
no kinks	104.8	105.0
TPCrefit	99.9	100.4
TRDrefit	79.3	77.6
TRDpidQuality=6	61.8	57.6

Table 6.4.: Average single track efficiencies within the p_T range $1\text{GeV}/c < p_T < 6\text{GeV}/c$ and pseudo-rapidity range $|\eta| < 0.8$.

As discussed above J/ψ mesons are reconstructed from electron and positron candidates each from the primary vertex and rapidity $|y| < 0.9$. The reconstruction efficiency is calculated analog to the single electron efficiencies. The result versus p_T is shown in Fig. 6.17 for the transverse momentum range $p_T < 6 \text{ GeV}/c$.

For $p_T < 1 \text{ GeV}/c$ the statistics is very low due to the initial p_T parameterisation of the J/ψ . The efficiency distribution continues to rise slowly without saturating in any of the investigated cases. At $p_T \gtrsim 1 \text{ GeV}/c$ a small drop sets in. The details of these distributions are still investigated. While the mean integrated efficiency for tracks with TPCrefit (magenta) in the range $1 < p_T < 6 \text{ [GeV}/c]$ is about 50% the ratio drops to about 25% for the additional TRDrefit (green) cut and even to less than 15% with the TRDpidQuality= 6 cut (blue). The exact numbers are listed in Table 6.5.

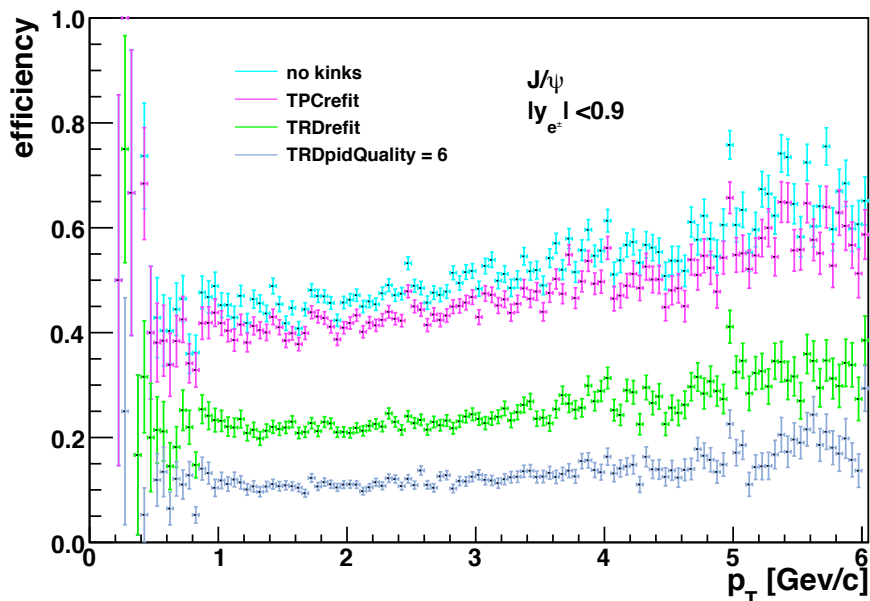


Figure 6.17.: J/ψ reconstruction efficiency in the p_T region $0 \text{ GeV}/c < p_T < 6 \text{ GeV}/c$.

The J/ψ reconstruction efficiency as a function of pseudo-rapidity shown in Fig. 6.18 saturates in the region $|\eta| < 0.5$ and stretches out to $|\eta| \approx 1.5$. In the almost constant efficiency region requiring the TPCrefit status bit set for both daughter tracks leads to an efficiency of about 65% while it decreases with requiring the TRDrefit to about 25% and requiring the TRDpidQuality= 6 to less than 20%.

Geometric effects like the gaps between the TRD stacks are not explicitly visible since two daughter tracks are taken into account. The loss of one of the daughter tracks reduces the overall J/ψ reconstruction rate, though. Additionally the η distribution of the initially decayed J/ψ Fig. 6.4 contributes.

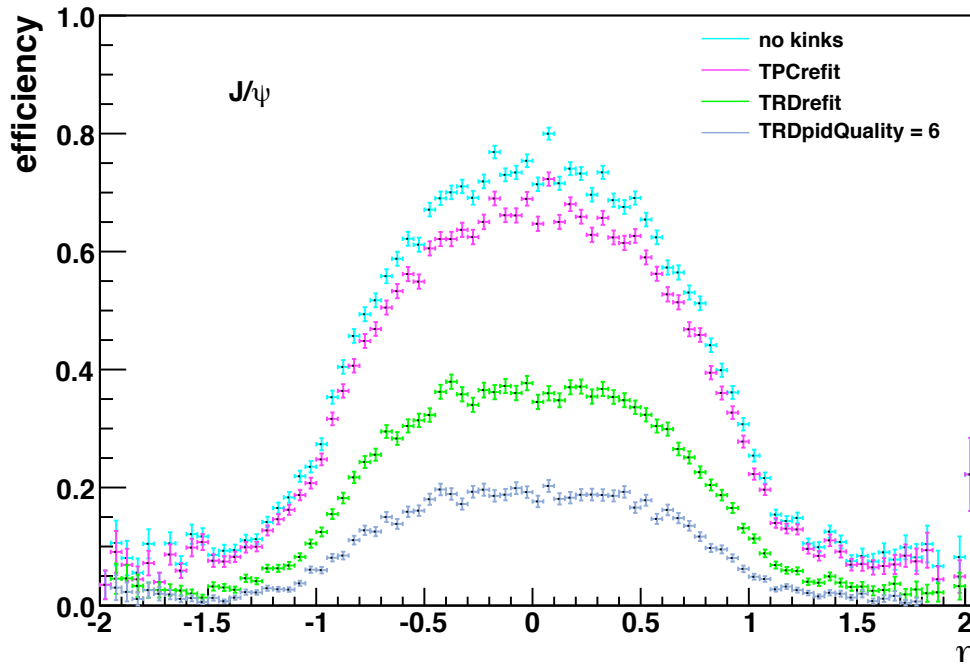


Figure 6.18.: J/ψ reconstruction efficiency in the pseudo-rapidity region $|\eta| < 2$.

cuts	efficiency [%]	
	p_T	η
no kinks	54.1	74.8
TPCrefit	48.5	67.6
TRDrefit	26.2	37.3
TRDpidQuality=6	13.7	19.5

Table 6.5.: Average J/ψ reconstruction efficiencies of the p_T range $1 < p_T < 6$ and pseudo-rapidity range $|\eta| < 0.5$.

Since PID information from TRD was not yet fully available in this thesis, electron identification is achieved via the MC truth information of a track for all result shown. A cut in the likelihood distribution accepting 90% of all reconstructed electron tracks is expected to keep the π efficiency to about 1%. Thus the results presented here were scaled by a factor of 0.9 for single track considerations and by a factor $0.9 \times 0.9 = 0.81$ for cases of involving invariant mass distributions.

6.5. Resolution

In this section an estimation on the resolution for the momentum and mass for J/ψ reconstruction with the ALICE central barrel is discussed.

Momentum Resolution

The momentum resolution of the ALICE central barrel is obtained as follows:

1. The difference between the MC input and the reconstructed p_T value

$$\Delta p_T = p_T^{MC} - p_T^{ESD}$$

is calculated as a function of p_T .

2. A Gaussian function is fitted for selected p_T bins in the range $|\Delta p_T| < 0.5$ GeV/ c , ignoring the Bremsstrahlungs tail of this distribution.
3. The width of the Gaussian function σ is obtained and plotted with its error as an absolute and relative value, see Fig 6.19 and Fig. 6.20.

The absolute resolution in GeV/ c as a function of p_T rises linearly from $\Delta p_T \approx 20$ MeV/ c to $\Delta p_T \approx 70$ MeV/ c in the considered range. With less bending radius the uncertainty of the measured radius increases at constant spatial resolution.

The relative resolution $\Delta p_T/p_T$ improves from about 2.5% to about 1.5% in the same p_T range when ignoring the entry at the lowest p_T . This is due to less multiple scattering of high-momentum particles.

The absolute values are systematically higher by 10 to 20 MeV/ c than shown in previous studies [50]. The relative momentum resolution shows a slightly different behaviour than in [50] since it is not deteriorate with p_T . Generally the values obtained in this work approach those of [50] for higher p_T .

Mass Resolution

To obtain the mass resolution of the detector as a function of transverse momentum, the invariant mass distribution for different slices of transverse momenta is taken. In selected p_T bins a Gaussian function is fitted in the mass range of $2.85 \text{ GeV}/c^2 < m < 3.25 \text{ GeV}/c^2$ ignoring the Bremsstrahlungs tail. The width σ of this Gaussian function versus p_T is shown in Fig. 6.21. An almost constant value of $\Delta m \approx 40$ GeV/ c^2 is found resulting in the full width of half maximum of the J/ψ peak of $FWHM = 2 \cdot \sqrt{2} \cdot \ln 2 \cdot \sigma \approx 94 \text{ MeV}/c^2$ and a relative resolution of $\Delta m/m \approx 3\%$. These results are in good agreement with those presented in [50] and [59] which were obtained from fast MC simulations, using parametrised functions for the detector response. For low transverse momenta $p_T < 1.5 \text{ GeV}/c$ the obtained values differ from the overall trend but suffer from low statistics.

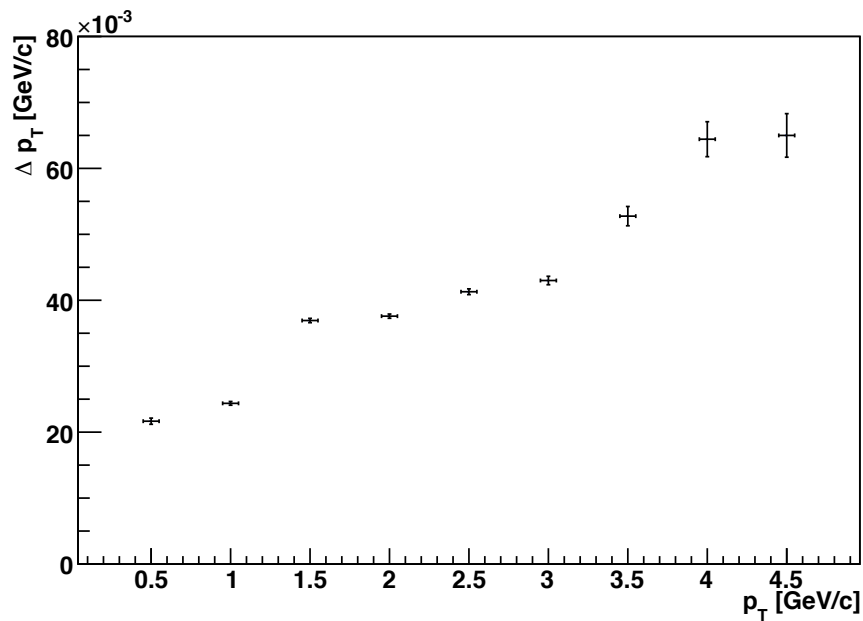


Figure 6.19.: Momentum resolution in GeV/c as a function of transverse momentum for electrons from J/ψ decay and rapidity $|y| < 0.9$.

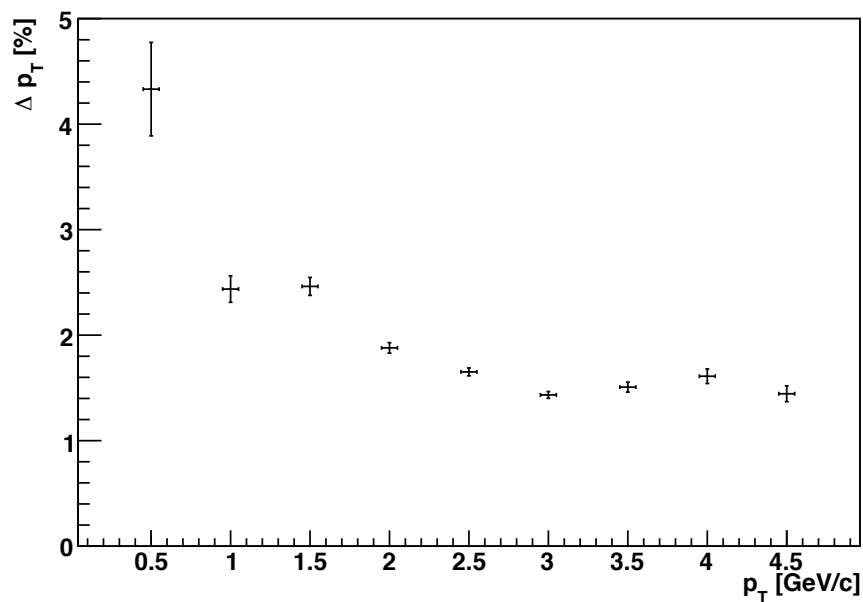


Figure 6.20.: Relative momentum resolution $\Delta p_T / p_T$ as a function of transverse momentum for electrons from J/ψ decay and rapidity $|y| < 0.9$.

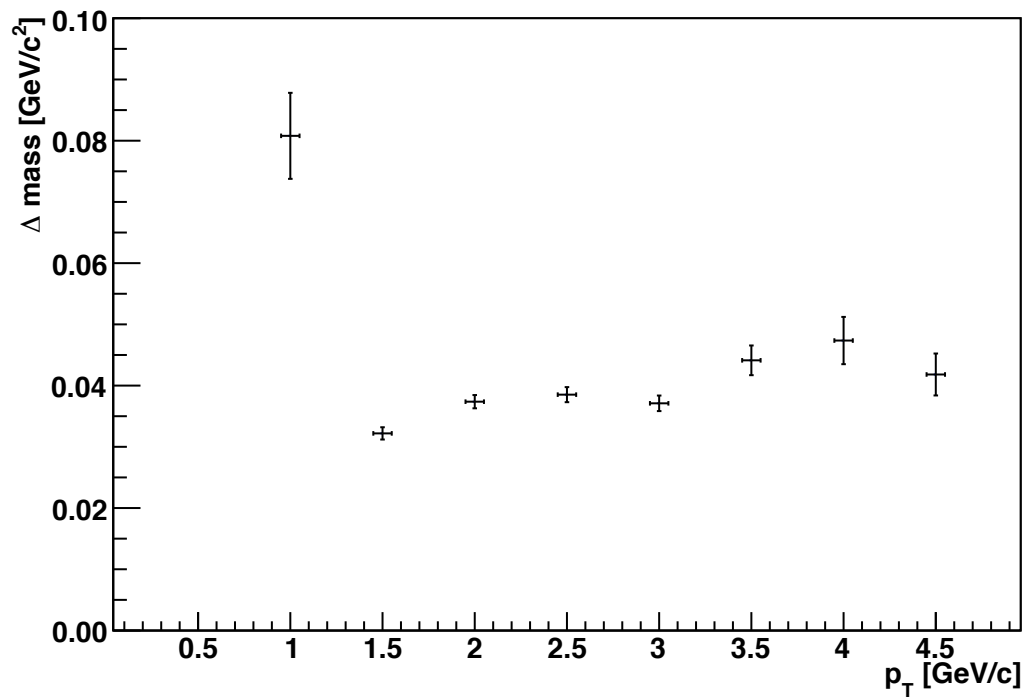


Figure 6.21.: Mass resolution as a function of transverse momentum for J/ψ reconstruction in the ALICE central barrel.

6.6. Background

In this section the combinatoric background of mis-identified hadrons e.g. π , K , p in $p+p$ collisions analog to experimental data is studied.

The simulation of *background* or minimum bias events is realised with PYTHIA and the settings:

- $p+p$ collisions
- center of mass energy 10 TeV
- natural decay rates
- p_T range of $0 - 1000 \text{ GeV}/c$
- rapidity range $-12 \leq y \leq 12$
- magnetic field $B = 0.5 \text{ T}$

- about 100k events

The invariant mass of these minimum bias events is calculated in a way similar to the one discussed above for the J/ψ signal. Single ESDtracks are selected according to the selection criteria:

- rapidity $|y| < 0.9$ as extracted from the reconstructed tracks
- no kinks
- TPCrefit
- TRDrefit
- TRDpidQuality = 6

The origin from the primary vertex is not explicitly required for the background invariant mass calculations. In order to minimize the computing time for simulation and data analysis, no PID restrains are applied, i.e. all particles not only electrons are used. Thus, the overall shape of the invariant mass distribution is the same as if electrons were selected but the statistics is far higher. The obtained background invariant mass distribution is afterwards scaled to the expected values. By estimating that 1% of the hadrons produced in $p+p$ collisions are misidentified as electrons this part of the scale factor is $1/(100 \times 100)$.

Furthermore only particles of the same charge are combined to the *like-sign* background. Using this method implies that the combined particles do not originate from the same physical process and are therefore uncorrelated. Thus, J/ψ mesons created in the minimum bias simulation are not reconstructed.

Additionally to the above discussed cuts several p_T cuts are applied to the single tracks.

Both the like-sign background and the J/ψ signal are normalised to 10^9 $p+p$ collisions. For the minimum bias events the scale factor is:

$$\text{Scale}_{BG} = \frac{1}{N_{events,BG}} \cdot N_{Coll} \cdot \left(\frac{1}{100}\right)^2$$

where $N_{events,BG}$ is the number of analysed minimum bias events. N_{coll} is listed in Tab. 6.6.

To obtain the scale factor for the signal the total number of produced J/ψ mesons in 10^9 $p+p$ collisions is estimated based on [58]:

$$\begin{aligned} \text{Scale}_{Sig} &= 1/N_{events,Sig} \cdot BR \cdot d\sigma/dy \cdot \Delta y \cdot \int \mathcal{L}dt \\ &= 1.62 \cdot 10^4 / N_{events,Sig} \end{aligned}$$

where $N_{events,Sig}$ is the number of produced J/ψ mesons and $BR \approx 0.06$ is the branching ratio of J/ψ decay into dielectrons, the other variables are listed in Tab. 6.6.

Figure 6.22. shows the fraction of reconstructed J/ψ mesons as a function of

quantity	value
\sqrt{s}	10 TeV
N_{coll}	10^9
σ_{pp}	70 mb
$\int \mathcal{L}dt$	15 nb^{-1}
$d\sigma/dy$	10 μb
Δy	1.8

Table 6.6.: Variables used for the scaling derived from [58].

the cut in transverse momentum of electrons (positrons). For $p_T = 0.5$ the same efficiency as shown above is reached. Further a strong influence of the p_T cuts is observed. The resulting absolute yields are summarised in Tab. 6.7.

created $J/\psi \cdot BR$	16200
rec. J/ψ , $p_T > 0 \text{ GeV}/c$	1805
rec. J/ψ , $p_T > 1.0 \text{ GeV}/c$	1235
rec. J/ψ , $p_T > 1.6 \text{ GeV}/c$	428

Table 6.7.: J/ψ yields for $J/\psi \rightarrow e^+ + e^-$ and rapidity $|y| < 0.9$ in 10^9 $p+p$ collisions.

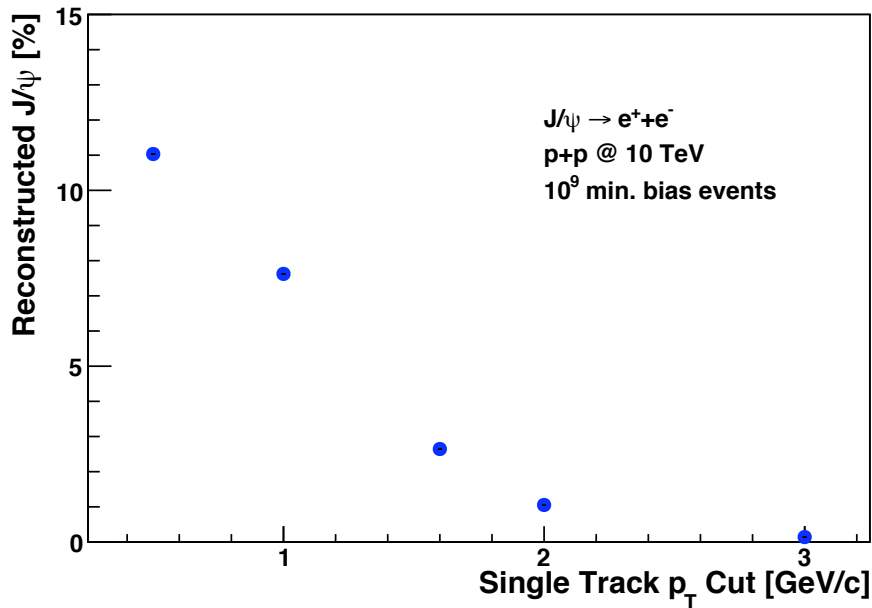


Figure 6.22.: Fraction of reconstructed J/ψ mesons as a function of the cut in transverse momentum of electrons (positrons).

Figure 6.23 shows the scaled signal (orange) as well as the total amount of reconstructed particles (blue), composed of the signal added to like-sign background. The single track cuts no kinks, TPCrefit , TRDrefit , $\text{TRDpidQuality} = 6$ are applied as discussed above. Additionally every track is required to have a transverse momentum $p_T > 1 \text{ GeV}/c$.

The integrated signal (S) to background (B) ratio in the invariant mass range from $3.08 \text{ GeV}/c^2$ to $3.12 \text{ GeV}/c^2$ is:

$$\frac{S}{B} = \frac{\sum N_{\text{signal}}}{\sum N_{\text{background}}} = 0.62$$

The obtained corresponding significance (SGN) is calculated

$$SGN = \frac{\sum N_{\text{signal}}}{\sqrt{\sum N_{\text{signal}} + \sum N_{\text{background}}}} = 18.3.$$

The signal to background ratio as a function of applied single track p_T cuts is shown in Fig. 6.24. Between $p_T = 0.5 \text{ GeV}/c$ and $p_T = 1.6 \text{ GeV}/c$ the signal to background value varies only little but rises rapidly for higher transverse momentum cuts. Accordingly the statistical significance of J/ψ reconstruction as a function of single track cuts in transverse momentum is shown in Fig. 6.25. While the significance is

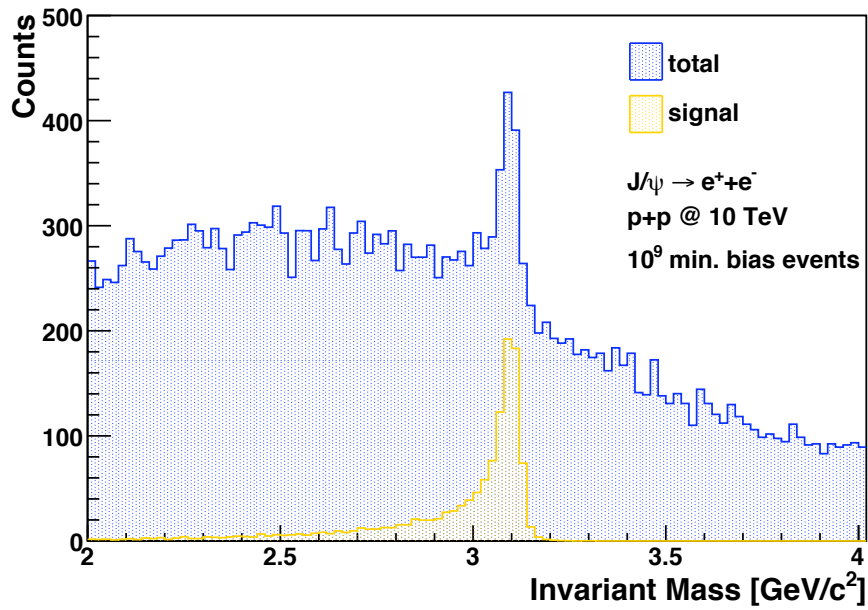


Figure 6.23.: Invariant mass distribution of the J/ψ signal (orange) and total = signal + like-sign background (blue) for 10^9 $p+p$ events after the single track cuts: no kinks, TPCrefit, TRDrefit, TRDpidQuality = 6 and $p_T > 1$ GeV/ c .

rather constant for a cut value up to 1.6 GeV/ c , it starts strongly decreasing for larger values. A detailed study on the J/ψ spectrum is under way.

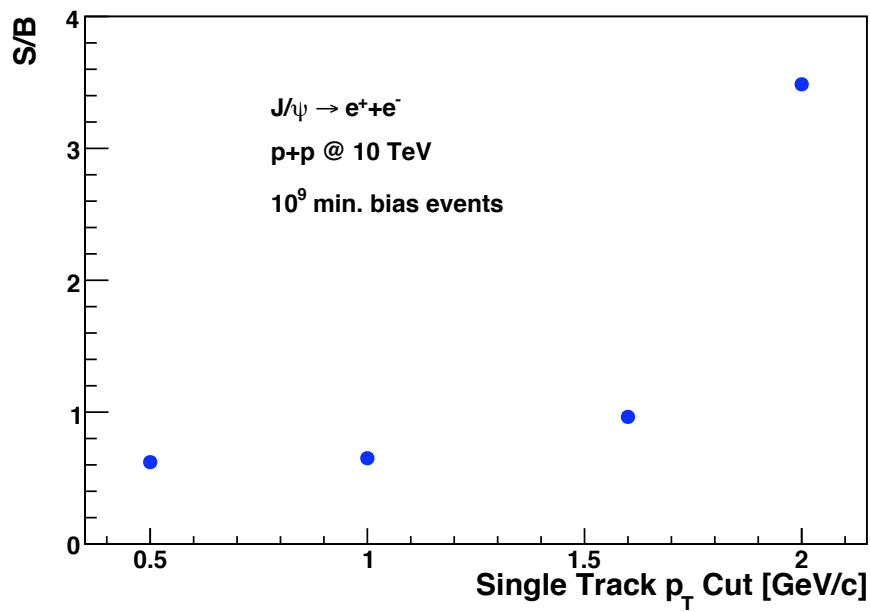


Figure 6.24.: Signal to Background ratio for different cuts on the single track transverse momentum.

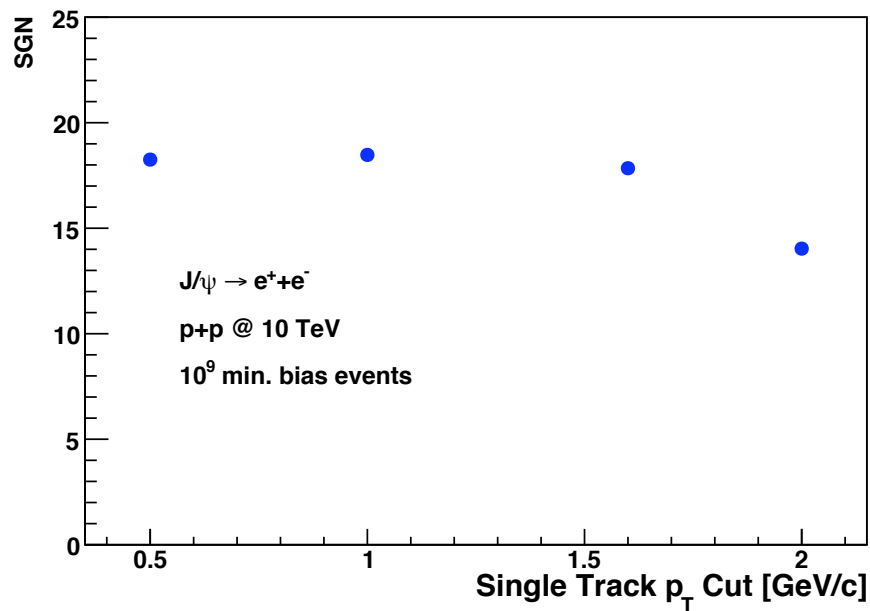


Figure 6.25.: Significance for different cuts on the single track transverse momentum.

7. Summary and Outlook

Within this thesis, the performance of J/ψ -production in $p+p$ collisions at $\sqrt{s} = 10$ TeV with the central barrel detectors in ALICE was studied. In particular, the decay channel $J/\psi \rightarrow e^+ + e^-$ ($BR \approx 6\%$) with the electron and positron identified by the Transition Radiation Detector using full-blown Monte Carlo simulations was examined. Influences of different cuts on reconstructed single tracks were carefully studied. Specially attention was given to select tracks with good particle identification.

When using the 2D likelihood method, the expected p_T dependence of the pion identification at 90% electron identification efficiency is observed. However, the cut-off value to select a 90 % electron PID efficiency strongly varies with the electron momentum.

Reconstruction of J/ψ mesons suffers from energy loss of the electron due to Bremsstrahlungs processes in the detector material. Roughly 30 % of all reconstructed J/ψ mesons appear in the tail of the invariant mass spectrum. This value is somewhat higher than in earlier studies, which found a 22 % contribution. The difference was attributed to overlapping volumes of the inner detector system with a forward detector leading to an effectively higher material budget. This feature is resolved in the latest version of the AliRoot Framework.

The efficiency for reconstructing J/ψ mesons is flat around 18% in $|\eta| < 0.5$ and linearly falling to 8% at $\eta = 0.9$. The overall efficiency at mid-rapidity is $\epsilon \approx 0.12$. This can be further increased by accepting e.g. single tracks with TRD information of five instead of six layers.

The momentum resolution of $\Delta p_T/p_T = 1.8\%$ and the mass resolution of $\sigma_{inv.mass} = 40$ MeV/ c^2 are in good agreement with earlier studies using fast simulations and parametrised function of the detector response.

With 10^9 $p+p$ collision, corresponding to 1 year of data taking with ALICE, roughly 1800 J/ψ mesons are expected to be reconstructed at a signal to background ratio of of 0.6. Within this thesis, combinatorial background from mis-identified hadrons was considered.

Future studies with even higher statistics will address correlated background from Drell-Yan processes and semi-leptonic decay of heavy-quark hadrons, e.g. $D\bar{D} \rightarrow e^+ + e^- + X$. Also, the subtraction of combinatorial background using the event-mixing technique is to be investigated.

First data from $p+p$ collisions at $\sqrt{s} = 10$ TeV at LHC will likely become available in the first half of 2009.

Bibliography

- [1] D.J. Gross and F. Wilczek, Phys. Rev. Lett. **30** (1973) 1343.
- [2] H.J. Politzer, Phys. Rev. Lett. **30** (1973) 1346.
- [3] N. Cabibbo and G. Parisi, Phys. Lett **B59** (1975) 67.
- [4] J.C. Collins and M.J. Perry, Phys. Rev. Lett. **33** (1975) 1353.
- [5] F. Karsch, Nucl. Phys. **A698** (1996) 199c;
F. Karsch, Lect. Notes Phys. **583** (2002) 209.
- [6] R. Hagedorn, Nuovo Cim. Suppl. **3** (1965) 147.
- [7] X. Zhu *et al.*, Phys. Lett. **B647** (2007) 366.
- [8] A. Andronic *et al.*, Nucl. Phys. **A789** (2007) 334.
- [9] L Yan, P. Zhuang and N. Xu, Phys. Rev. Lett. **97** (2006) 232301.
- [10] M. Djordjevic and M. Gyulassy, Acta. Phys. Hung. **A24** (2005).
- [11] B. Zhang, L.W. Chen and C-M. Ko, Phys. Rev. **C72** (2005).
- [12] P. Braun-Munzinger and J. Stachel, Nucl. Phys. **A690** (2001) 119c.
- [13] A. Andronic *et al.*, Phys. Lett. **B571** (2003) 36.
- [14] H. Satz and T. Matsui, Phys. Lett. **B178** (1986) 416.
- [15] M.C. Abreu *et al.*, Phys. Lett. **B499** (2001) 85.
- [16] A. Capella, A.B. Kaidalov and D. Sousa, Phys. Rev. **C65** (2002) 054908.
- [17] P. Braun-Munzinger and J. Stachel, Phys. Lett. **B490** (2000) 196.
- [18] R.L. Thews, M. Schroedter and J. Rafelski, Phys. Rev. **C63** (2001) 054905.
- [19] L. Grandchamp *et al.*, Phys. Rev. **C73** (2006) 064906.
- [20] B. Zhang, Phys. Lett. **B647** (2007) 249.
- [21] V. Greco, C.M. Ko, R. Rapp, Phys. Lett. **B595** (2004) 202.
- [22] Z.W. Lin and D. Molnar, Phys. Rev. **C68** (2003) 044901.
- [23] A. Andronic *et al.*, Phys. Lett. **B652** (2007) 259.
- [24] A. Adare *et al.*, Phys. Rev. Lett. **98** (2007) 232301.
- [25] A. Mocsy; 417th WE-Heraeus-Seminar.

- [26] I. Vitev and M. Gyulassi, Phys. Rev. Lett. **89** (2002) 252301.
- [27] P. Jacobs and X. Wang, Prog. Part. Nucl. Phys **54** (2005) 443.
- [28] R. Vogt, Eur. Phys. **J** **155** (2008) 213.
- [29] A. Suaide, J. Phys. G: Nucl. Part. Phys. **34** (2007) S369.
- [30] K. Yagi *et al.*, *Quark-Gluon Plasma*, (Cambridge Univ. Press, 2004).
- [31] R. Soualah, *private communication*.
- [32] F.Karsch, BI-TP 2001/06 (2001).
- [33] T. Hatsuda, J. Phys. **G**: Nucl. Part. Phys. **34** (2007) S287.
- [34] Y. Aoki *et al.*, Nature **443** (2006) 675.
- [35] A. Mocsy and P. Petreczky, Phys. Rev. Lett. **99** (2007) 211602.
- [36] J. J. Aubert, *et al.*, Phys. Rev. Lett. **33** (1974),1404.
- [37] J. E. Augustin, *et al.*, Phys. Rev. Lett. **33** (1974),1406.
- [38] D. H. Perkins, *Introduction to High Energy Physics*, (University Press, Cambridge, 2000).
- [39] A. Wachter and H. Hoerber, *Repetitorium Theoretische Physik*, (Springer, 2005).
- [40] H. Satz, J. Phys.**G** **32** (2006), R25.
- [41] Particle Data Group, C. Amsler *et al.*, Phys. Lett. **B** **667** (2008) 1.
- [42] W. H. Smith, *LHC startup*, arXiv:0808.3131 [hep-ex].
- [43] LHC webpage, <http://lhc.web.cern.ch/lhc/>.
- [44] ALICE Collaboration, ALICE: Physics Performance Report, Volume I, J. Phys. **G** **30** (2004) 1517.
- [45] ALICE Collaboration, ALICE TDR 010, CERN-LHCC-2003-062 (2004).
- [46] P. Giubellino, Heavy Ion Physics at the LHC, arXiv:0809.1062 [nucl-ex].
- [47] ALICE Collaboration, ALICE: Physics Performance Report, Volume II, J. Phys. **G** **32** (2006) 1295.
- [48] A. Wilk, Nucl. Instrum. Meth. **A** **563** (2006) 314.
- [49] A. Wilk, Diploma Thesis, University of Münster (2004).
- [50] W. Sommer, Dissertation, University of Frankfurt (2008).
- [51] ROOT User's Guide, <http://root.cern.ch/root/doc/RootDoc.html>.
- [52] H-U. Bengtsson and T. Sjostrand, Comput. Phys. Commun. **46** (1987) 43;
T. Sjostrand, Comput. Phys. Commun. **82** (1994) 74.
- [53] X-N. Wang and M. Gyulassy Phys. Rev. **D** **44** (1991) 3501;
M. Gyulassy and X-N. Wang Comput. Phys. Commun. **83** (1991) 307-31.

- [54] P. Hristov, AliRoot Primer.
- [55] P. Billoir, Nucl. Instr. Meth. **A225** (1984) 352;
P. Billoir et al., Nucl. Instr. Meth. **A241** (1984) 115;
R. Fruhwirth, Nucl. Instr. Meth. **A262** (1987) 444;
P. Billoir, Comput. Phys. Commun. **57** (1989) 390.
- [56] ALICE Collaboration, ALICE TDR 012, CERN-LHCC-2005-018 (2005).
- [57] S. Gorbunov and I. Kisel., CBM-SOFT note 2007-003.
- [58] A. Andronic *et al.*, Nucl. Phys. **A 798** (2007) 334.
- [59] F. Kramer, Diploma Thesis, University of Frankfurt (Main).

Acknowledgments

First and foremost I would like to express my gratitude to my supervisor Dr. Kai Schweda for providing me with this interesting topic. His enthusiasm and advice were a constant encouragement.

I'm thankful that Professor Dr. Schultz-Coulon agreed to be the second corrector of this thesis.

Sylwester Radomski I would like to thank for constant help in many matters e.g. with AliRoot and physics questions.

Furthermore I would like to thank:

Sylvia Masciocchi for helping with AliRoot questions and for the simulation of the minimum bias data at the GSI cluster.

Minjung Kweon for help with AliRoot and with the usage of Condor and the HD cluster.

WooJin Park, Yifei Wang and Ana Marin for various help and discussions.

Alexandru Bercuci, Alexander Wilk and Markus Fasel for their explanations and efforts concerning the PID.

Yvonne Pachmeier for proofreading this thesis.

Special thanks go to my family for their encouragement and support, that made my studies possible.

Finally, representative for others, I would like to thank the thursday table group for providing distraction and amusement.

This work has been supported by the Helmholtz Association under contract number VH-NG-147 and and the Federal Ministry of Education and Research under promotional reference 06HD197D.

Erklärung

Ich versichere, dass ich diese Arbeit selbständig verfasst und keine anderen als die angegebenen Quellen und Hilfsmittel benutzt habe.

Heidelberg, den 30.10.2008

.....

Dirk Krumbhorn